Revista Mexicana de Astronomía y Astrofísica, **32**, 3–26 (1996)

EMISSION LINE IMAGES AND SPECTRA OF ASYMMETRIC BOWSHOCKS

W.J. Henney

Instituto de Astronomía
Universidad Nacional Autónoma de México

Received 1995 August 25; accepted 1995 November 21

RESUMEN

Se investiga la forma y las propiedades emisivas de choques de proa asimétricos usando modelos analíticos. Se consideran dos orígenes para la asimetría: 1) un gradiente de densidad transversal en el medio por lo cual se propaga el choque de proa; 2) un sesgo en la distribución del gas del chorro chocado que está impulsando el choque de proa. En cada caso, se presentan imágenes y diagramas de posición-velocidad para líneas de emisión tanto de alta como de baja excitación. Se aplican estos modelos a observaciones de choques de proa en las cabezas de chorros de estrellas jóvenes. Se encuentra que, en el caso de Herbig-Haro 1, la causa más probable de la asimetría observada en este objeto es un gradiente de densidad ambiental.

ABSTRACT

The shape and emission properties of asymmetric radiative bowshocks are investigated using analytic models. Two origins for the asymmetry are considered: 1) a transverse density gradient in the ambient medium into which the bowshock is propagating; 2) a skewness in the pressure distribution of the shocked jet gas that is driving the bowshock. In each case, images and position-velocity diagrams are presented for both high- and low-excitation emission lines. These models are applied to observations of bowshocks at the heads of jets from young stars. It is found that, in the case of Herbig-Haro 1, an ambient density gradient is the most likely cause of the asymmetry observed in this object.

Key words: **HYDRODYNAMICS — ISM – INDIVIDUAL (HH 1) — ISM – JETS AND OUTFLOWS — LINE – PROFILES**

1. INTRODUCTION

Herbig-Haro (HH) objects were originally discovered as knots of optical line emission, found in regions of low mass star formation (Herbig 1951; Haro 1952). However, they are now observed in all spectral regions from radio to ultraviolet and similar objects have been associated with high mass stars (Martí, Rodríguez, & Reipurth 1993). Recent reviews of observations include Reipurth (1992) and Rodríguez (1989). A useful database is given by Reipurth (1994).

HH objects are often found in groups, arranged in linear or quasi-linear structures, frequently with aligned proper motion vectors (Herbig & Jones 1981; Reipurth, Raga, & Heathcote 1992; Eislöffel, Mundt, & Böhm 1994) and are widely believed to be a manifestation of the collimated supersonic ejection of material from young stars or their close circumstellar environs. They show an emission line spectrum characteristic of shockwaves, with velocities typically in the range 50–200 km s^{-1} (Schwartz & Dopita 1980) and, in many cases, individual knots or groups of knots have shapes that are very suggestive of bowshocks (e.g., HH 1, HH 34, HH 46/47, HH 111). These latter objects have traditionally been interpreted as the result of the stellar ejecta impinging on the ambient medium, with the ejecta either being in a continuous collimated wind or jet (Cantó & Rodríguez 1980; Cantó, Tenorio-Tagle, & Różyczka 1988), or consisting of discrete blobs or cloudlets (Schwartz 1975; Norman & Silk 1979). More recently, variable speed jet models, in which internal

bowshocks form along the length of the jet, have had great success in explaining observations of some objects (Raga et al. 1990; Raga & Kofman 1992). Much work has been done on modelling the dynamics and emission of radiative bowshocks (Raga 1985; Hartigan, Raymond, & Harthmann 1987; Raga 1988; Hartigan 1989; Noriega-Crespo, Böhm, & Raga 1990) and on comparing predicted morphology, kinematics and spectra with observations of HH objects (Choe, Böhm, & Solf 1985; Noriega-Crespo, Böhm, & Raga 1989; Solf et al. 1991; Morse et al. 1992; Raga & Noriega-Crespo 1993; Indebetouw & Noriega-Crespo 1995). However, to date, all such studies have assumed cylindrical symmetry for the bowshock structure.

Interaction between supersonic stellar ejecta and ambient gas will result in the formation of two shocks (Pikelner 1968; Dyson & deVries 1972), separated by a contact discontinuity. The outer shock accelerates the ambient gas, while the inner shock decelerates the ejecta. In the case where the ejecta is a jet, the inner shock is called the Mach disk and the outer shock the bowshock. Depending on the velocity of the jet and the density ratio between the jet and the ambient medium, either or both of the bowshock and Mach disk may be radiative (Hartigan 1989). In this paper, a preliminary study is presented of the emission properties of bowshocks that depart from cylindrical symmetry. This asymmetry is considered to be the result either of perturbations in the density of the medium into which the bowshock is propagating or of asymmetries in the jet that is driving the bowshock, possibly resulting from temporal variations in the jet direction. Very simple analytic steady-state models are employed and these are described in § 2. The method of calculating the bowshock emission, together with an examination of the validity of some of the model assumptions, is presented in § 3, while resultant images and spectra of selected optical emission lines are illustrated in § 4 and § 5, respectively. The application of these models to actual objects is then considered in § 6.

2. CALCULATION OF THE BOWSHOCK SHAPE

2.1. General Treatment

Consider a bowshock formed by the interaction with an inhomogeneous environment of a jet travelling along the z-axis. We assume that the shocked jet material does not cool but forms a cocoon with a thermal pressure P, and that both P and the density ρ of the ambient medium in front of the bowshock are independent of z. On the other hand, the ambient gas is assumed to cool promptly after passing through the bowshock, forming a thin, shocked layer (see § *3.1.* for discussion of the validity of these assumptions). Then, ignoring centrifugal and Coriolis forces, we can balance the cocoon pressure with the ram pressure of gas entering the bowshock to obtain

$$P(x,y) = \rho(x,y)\left[\mathbf{u}.\hat{\mathbf{n}}(x,y)\right]^2 \quad , \tag{1}$$

where $\mathbf{u} = u_0\hat{\mathbf{k}}$ is the pattern speed of the bowshock and $\hat{\mathbf{n}}(x,y)$ is the unit vector normal to the bowshock surface.

The shape of the bowshock surface can be described by a function $f(x,y,z)$, such that $f = 0$ on the surface. We can also choose that $|\nabla f| = 1$ on the surface, so that we have $\hat{\mathbf{n}} = \nabla f$. Hence, equation (1) can be rewritten

$$f_z^2 = \frac{P}{\rho u_0^2} \quad , \tag{2}$$

that is, f_z is independent of z (the subscripts here indicate partial differentiation). Hence, we can write

$$f(x,y,z) = \frac{1}{u_0}\sqrt{\frac{P}{\rho}}\left[z + g(x,y)\right] \quad , \tag{3}$$

where $g(x,y)$ is a solution of the partial differential equation

$$g_x^2 + g_y^2 = \frac{\rho u_0^2}{P} - 1 \quad . \tag{4}$$

The shape of the bowshock is then given by

$$z = -g(x,y) \quad . \tag{5}$$

2.2. Specific Solutions

In this section, three particular cases will be considered in which explicit solutions for g in equation (4) can be found by analytic means.

Case 0. The symmetrical case, in which the preshock density is constant and the jet pressure is a function solely of cylindrical radius from the z-axis, leading to a cylindrically symmetric bowshock.

Case 1. The case of a non-uniform ambient medium, in which there is a transverse density gradient in the preshock gas.

Case 2. The case of a skew jet, in which the pressure of the shocked jet gas falls off in an asymmetric way with distance from the jet axis.

Cases 1 and 2 are illustrated schematically in Figure 1. In each case, the preshock gas is assumed to be at rest or to have a constant velocity aligned with the jet axis (which amounts to the same thing so long as all velocities are considered to be with respect to this gas). Of course, another way to generate

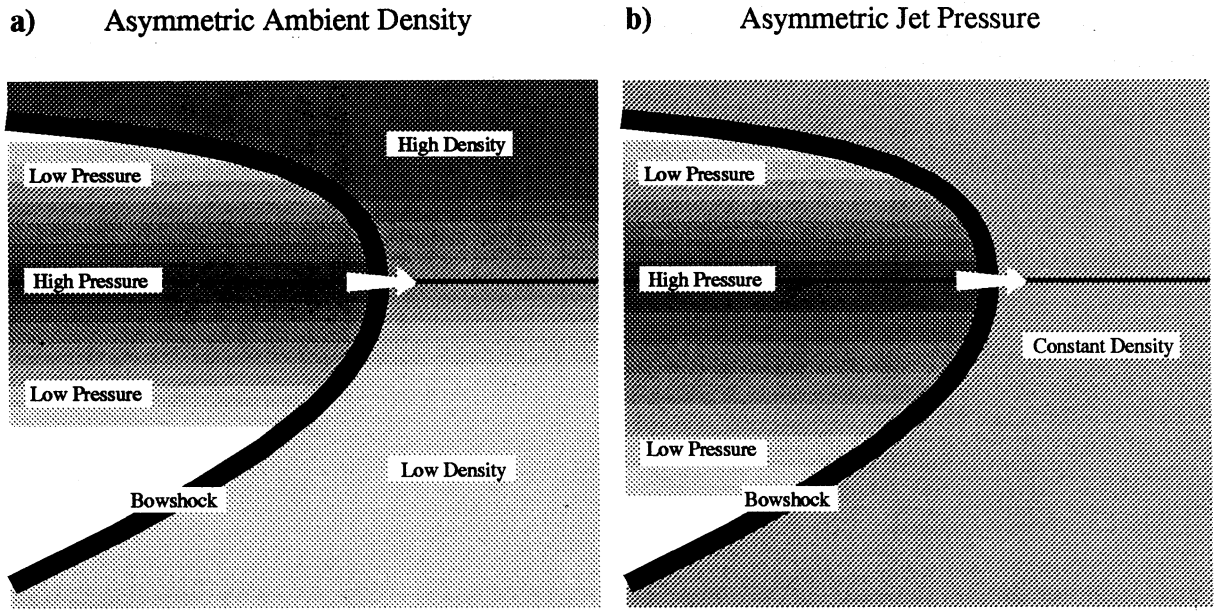

Fig. 1. A steady-state asymmetric bowshock may be caused *(a)* by a density gradient in the ambient medium or *(b)* by a non-axisymmetric pressure distribution in the shocked jet.

an asymmetrical bowshock would be for the preshock gas to have a non-zero velocity component transverse to the jet axis (e.g., narrow-angle-tail radio galaxies, Balsara & Norman 1992) or a parallel component that varied with position. However, this possibility will not be pursued further here, apart from a brief discussion in § *A.2*, where it will be shown that it would present considerable problems for the method employed in calculating the bowshock emission.

2.2.1. Case 0: Symmetrical Bowshock

We will consider the following form for the pressure of the shocked jet material

$$P = \frac{P_0}{1 + (x^2 + y^2)^{\xi}} \quad , \tag{6}$$

where P_0 is the on-axis pressure and ξ (> 0) measures how steeply the pressure falls with distance from the axis. This is probably a reasonable parameterization of realistic jet pressure distributions except for far from the jet axis, where the approximation of balancing shocked jet gas thermal pressure against the ram pressure of incoming ambient gas breaks down anyway.

In this case ($\rho = \rho_0$), the bowshock will be cylindrically symmetric and equations (4), (5), and (6) are easily solved (with the requirement that the cross sections through the bowshock at each z be closed curves) to give the shape

$$z = -\frac{1}{1+\xi}\,(x^2 + y^2)^{(1+\xi)/2} \quad . \tag{7}$$

For $\xi = 1$, this implies a paraboloid bowshock, whereas larger or smaller values of ξ give respectively blunter or more pointed bowshocks, as one would expect.

2.2.2. Case 1: Non-Uniform Ambient Density

Using the the same jet pressure distribution as in the previous case, it follows that, if the shape of the bowshock $g(x, y)$ is given, then, with the requirement that the apex of the bowshock lies on the z-axis (so that $P = \rho u_0^2$ there), the ambient density distribution is given by

$$\rho = \rho_0 \frac{1 + g_x^2 + g_y^2}{1 + (x^2 + y^2)^{\xi}} \quad , \tag{8}$$

where ρ_0 is density on the z-axis. We only consider density distributions that possess mirror symmetry about the plane $y = 0$, which implies $g_y = 0$ on this mid-plane. Hence, using equation (4), we can write the pressure balance in the mid-plane as

$$g_x^2 = \frac{u_0^2}{P_0}\,(1 + x^{2\xi})\,\rho(x, 0) - 1 \quad . \tag{9}$$

Since g_x^2 must be positive for all values of x, this constrains the possible mid-plane density distributions

$\rho(x,0)$. In particular, exponential density profiles or power-law profiles with exponents of 2ξ or greater cannot give rise to a bowshock shape that is valid for all x.

Rather than directly choose a form for $\rho(x,0)$, we instead, by analogy with the results in the previous case, choose g in the mid-plane to be

$$g(x,0) = \left(\frac{1+\mathcal{D}\tanh x}{1+\xi}\right) x^{1+\xi} \quad , \qquad (10)$$

where $\mathcal{D}$ is a measure of the asymptotic density contrast between the two sides of the mid-plane. This has the desirable property that $g(x) \rightarrow (1 \pm \mathcal{D})\, x^{1+\xi}/(1+\xi)$ as $x \rightarrow \pm\infty$. In other words, away from the jet axis, the bowshock shape in the mid-plane will have the same functional form as in the symmetrical case, but will be more "open" on one side than the other. Then, using equation (9), the mid-plane ambient density can be found as

$$\rho(x,0) = \rho_0 \left\{\frac{1+\left[x^{\xi} h(x)\right]^2}{1+x^{2\xi}}\right\} \quad , \qquad (11)$$

where

$$h(x) = 1 + \frac{\mathcal{D}}{1+\xi}\left[(1+\xi)\tanh x + x\,\mathrm{sech}^2 x\right] \quad . \qquad (12)$$

This gives a "triple-plateau" density distribution, where the density to either side of $x = 0$ tends towards

$$\rho_{\pm} \equiv \lim_{x\rightarrow\pm\infty}\left[\rho(x,0)\right] = (1 \pm \mathcal{D})^2 \rho_0 \quad . \qquad (13)$$

This is illustrated in Figure 2 for $\mathcal{D} = 0.3$ and for three values of ξ (0.5, 1.0 and 2.0), together with the corresponding bowshock shapes.

To find the solution away from the plane $y = 0$, we assume that $\rho = \rho_0$ everywhere in the plane $x = 0$. Hence, if we require that we recover the Case 0 solution when $\mathcal{D} \rightarrow 0$, then one of the simplest solutions is

$$g(x,y) = \frac{(1+\mathcal{D}\tanh x)\left(x^2+y^2\right)^{(1+\xi)/2}}{1+\xi} \quad . \qquad (14)$$

This implies that the density distribution is

$$\rho(x,y) = \rho_0 \left[\frac{1+B(x,y)\left(x^2+y^2\right)^{\xi}}{1+\left(x^2+y^2\right)^{\xi}}\right] \quad , \qquad (15)$$

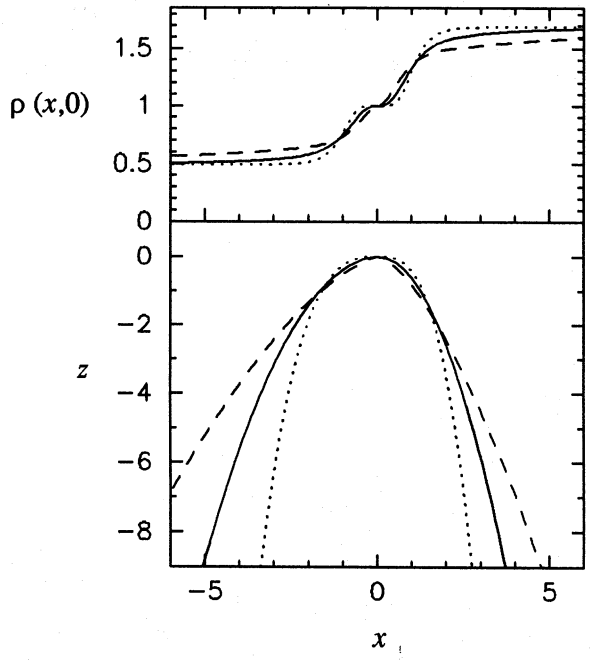

Fig. 2. Mid plane density profiles (upper panel) and corresponding xz-sections through the bowshock shape (lower panel). Density contrast $\mathcal{D} = 0.3$, cocoon pressure index $\xi = 0.5$ (dashed line), 1.0 (solid line), 2.0 (dotted line).

where

$$B(x,y) = (1+\mathcal{D}\tanh x)^2 + \frac{2x\mathcal{D}\,\mathrm{sech}^2 x}{1+\xi}(1+\mathcal{D}\tanh x) + \frac{\mathcal{D}^2\,\mathrm{sech}^4 x}{(1+\xi)^2}\left(x^2+y^2\right) \quad . \qquad (16)$$

This density distribution, together with contours of xy slices through the corresponding bowshock shape, is illustrated in the top panels of Figure 3 for $\xi = 1$ and 2. It can be seen that, in each case, the distribution is close to plane-parallel. Note that at radii larger than those illustrated the density is rather ill-behaved, developing peaks in the $x = 0$ plane. However, this does nor affect any of the models calculated here.

2.2.3. Case 2: Skew Jet Pressure

Since there are virtually no a priori constraints on reasonable functional forms for the jet pressure in this case, we are even more justified than in the previous case in working backwards from an assumed bowshock shape. It is found that a reasonable choice is

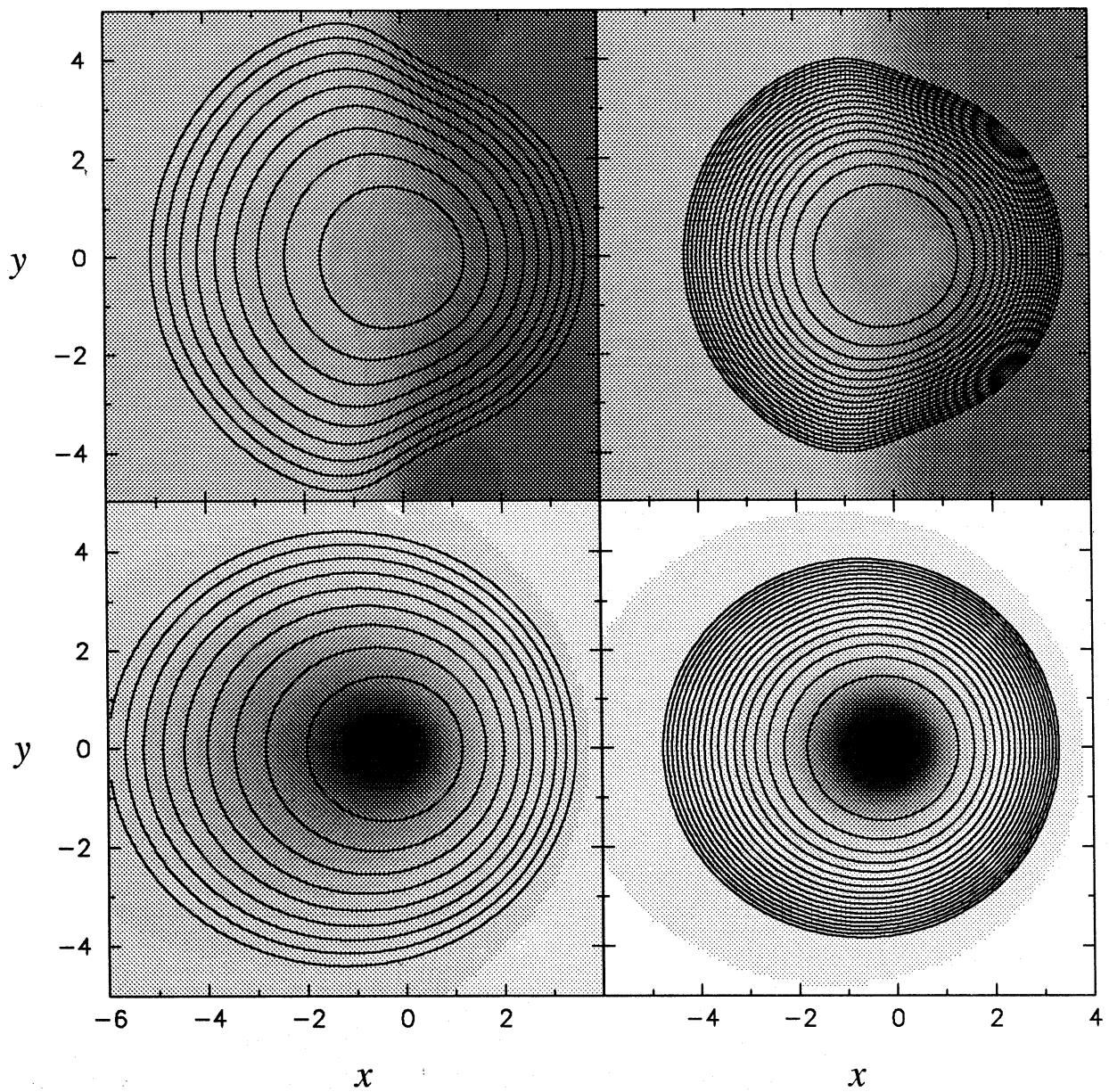

Fig. 3. The ambient density (top panels) or shocked jet pressure (bottom panels) in any xy plane (grayscale) with superimposed xy-sections through the bowshock shape (solid lines). Top panels are for Case 1 models with density contrast parameter $\mathcal{D} = 0.3$, bottom panels are Case 2 models with pressure skewness parameter $a = 0.5$. Left-hand panels show paraboloid models with shape parameter $\xi = 1$, right-hand panels show blunter models with $\xi = 2$. The xy-sections are shown for integer values of z, starting at $z = 1$. The density and pressure scales are linear.

$$g = \left(\frac{1 + a\cos\theta}{1+\xi}\right) r^{1+\xi} \quad , \tag{17}$$

where $r = (x^2 + y^2)^{1/2}$, $\theta = \tan^{-1}(x/y)$ and a describes the severity of the skewness. From the cylindrical-polar analogue of equation (4), assuming constant ambient density, we have

$$P/P_0 = (1 + g_r^2 + g_\theta^2/r^2)^{-1} \quad , \tag{18}$$

from which the pressure distribution is found to be

$$P = \frac{P_0}{1 + A(\theta) r^{2\xi}} \quad , \tag{19}$$

where

$$A(\theta) = (1 + a\cos\theta)^2 + a^2 \sin^2\theta/(1+\xi)^2 \quad . \quad (20)$$

Note that when $a = 0$, then $A = 1$ and equation (19) reduces to equation (6) as required. This pressure distribution is illustrated in the bottom panels of Figure 3.

3. CALCULATION OF THE BOWSHOCK EMISSION

The emission from the bowshock is calculated using a probabilistic technique, in which points of origin for photons on the bowshock surface are selected randomly from a given probability distribution. The main reason for adopting this approach is to allow the calculation of the scattering of the bowshock emission lines by surrounding dust. These calculations, using a modification of the Monte Carlo scattering algorithm described in Hennney & Axon (1995), will be published in a subsequent paper. The formalism is only tangentially relevant for the purposes of the current paper and is hence described in an Appendix. The emission per unit area at each point on the bow shock surface is taken from the pre-ionized shock models of Hartigan et al. (1987), using the local values of the shock velocity and pre-shock density.

The assumption of prompt post-shock cooling is examined in § *3.1.* and the post-shock gas velocity distribution (required for the construction of spectra) is discussed in § *3.2.*

3.1. Cooling Lengths

We will now discuss the length scales on which gas is expected to cool behind the bowshock, in order to justify the assumptions made in calculating the bowshock emission. The characteristic time for gas of pressure P to cool at a rate L (erg s^{-1} cm^{-3}) is given by

$$t_c = \frac{P}{(\gamma - 1)L} \quad , \quad (21)$$

where γ is the adiabatic index. Using straight-line fits to the cooling function on the three temperature intervals, (*i*) $< 10^4$ K; (*ii*) $10^4 - 10^5$ K, and (*iii*) $> 10^5$ K (Kahn 1976; Arthur, Dyson, & Hartquist 1993), we obtain the following expressions for the postshock cooling time in terms of the perpendicular shock velocity v_{100} (in units of 100 km s^{-1}) and the preshock density n_{100} (in units of 100 cm^{-3})

$$t_c = \begin{cases} 4.810 \times 10^{-4}\, n_{100}^{-1}\, v_{100}^{-6} \text{ yrs } (v_{100} < 0.211) \\ 4.04\, n_{100}^{-1}\, v_{100}^{-0.2} \text{ yrs } (0.211 < v_{100} < 0.666) \\ 14.85\, n_{100}^{-1}\, v_{100}^{3} \text{ yrs } (v_{100} > 0.666) \quad . \end{cases} \quad (22)$$

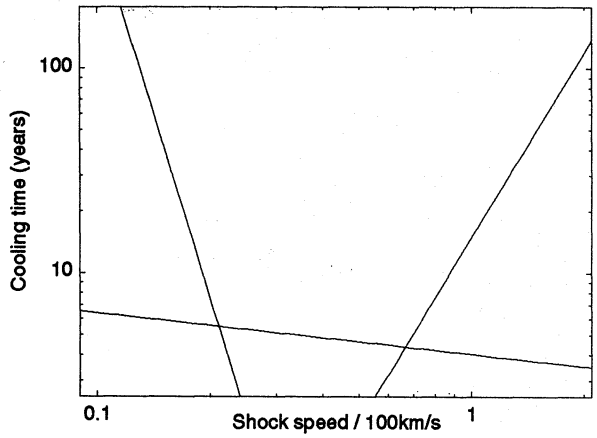

Fig. 4. Cooling time as a function of shock velocity for a preshock density of 100 cm^{-3}.

This cooling time is illustrated in Figure 4. We can now roughly estimate the cooling distances, both parallel and perpendicular to the shock as

$$d_\parallel = 1.02 \times 10^{-4}\, w_{100}\, t_c \text{ pc} \, , \quad (23)$$

$$d_\perp = 1.02 \times 10^{-4}\, (0.25\, v_{100})\, t_c \text{ pc} \, , \quad (24)$$

where w_{100} is the velocity of postshock gas parallel to the shock front, which is equal to the parallel component of velocity with which the gas enters the shock (note that these velocities are all specified in the frame in which the bowshock is stationary). This value for $d_\perp$ is an upper limit, since the normal velocity component of the gas will decrease from $0.25 v_{100}$ to roughly zero as the postshock gas cools. However, fits to the cooling distances in numerical shock models Raga & Binette 1991) give similar results. On the other hand $d_\parallel$ should quite closely reflect how far along the bowshock the gas travels before cooling, although a precise estimate would require a detailed calculation of the postshock flow. Figure 5 shows these cooling distances for a high-speed (175 km s^{-1}) and a low-speed (50 km s^{-1}) bowshock model, with and without an ambient density gradient. The unit of length for the models (scale length of shocked jet pressure distribution, see eq. (1) is taken to be 2.18×10^{-3} pc, which gives bowshock sizes typical of those found in HH objects.

For the high-speed symmetric model, $d_\parallel$ is zero at the head of the bowshock ($x = 0$) because w, the parallel component of the postshock velocity, is zero there. To each side, w increases monotonically towards the wings but the perpendicular shock velocity v decreases, leading to a rapid fall in t_c (since we are on the right hand side of Fig. 4), leading to a maximum in $d_\parallel$ near the head. On the other hand, $d_\perp$

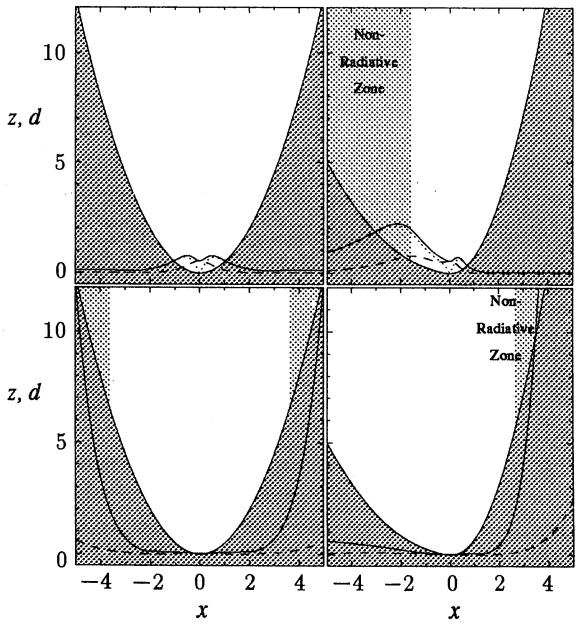

Fig. 5. Cooling distances behind the bowshock, $d_\parallel$ (dotted line) and $d_\perp$ (dashed line), together with total cooling distance $(d_\parallel^2 + d_\perp^2)^{1/2}$ (solid line). Also shown are $y = 0$ cuts through the bowshock shape (solid line bounded by dark gray shaded area). Top panels show a model with bowshock pattern speed $u_0 = 175$ km s^{-1} and preshock density $n_0 = 300$ cm^{-3}; bottom panels show a model with $u_0 = 50$ km s^{-1}, $n_0 = 100$ cm^{-3}. In both models, the unit of length is taken to be 2.18×10^{-3} pc. Left panels have $\mathcal{D} = 0$, right panels have $\mathcal{D} = 0.6$. Light gray shaded area indicates where the total cooling length exceeds 2.

peaks at $x = 0$ and falls off to each side, due to the decrease in both v and t_c. The total cooling distance never rises above 1 for this model, so the assumption of strong cooling and strictly local emission behind the bowshock is well justified.

For the asymmetric version of the same model, a similar pattern is seen except that the cooling time (proportional to n^{-1}) increases on the low density side, causing $d_\parallel$ to exceed unity there. This means that the postshock gas no longer cools immediately at the position where it enters the shock, but only after it has been carried some way downstream. The resultant expansion cooling and geometric dilution will reduce the brightness of emission from this side of the bowshock, but by an amount that is hard to estimate without performing full hydrodynamic calculations. In the figure, the region downstream of where $d_\parallel > 2$ is designated a non-radiative zone (although the choice of 2 is somewhat arbitrary). The low-speed model behaves quite differently since the relevant range of v is in the central part of Figure 4 and hence t_c is almost completely insensitive to v, except for when v falls to very low values, leading to long cooling lengths only in the far wings of the bowshock where the emission is very faint anyway.

In the models presented here, the Mach disk (jet shock) is assumed to be non-radiative so that its emission can be ignored. This is not necessarily a good approximation for many HH objects, although we will now show that it is probably valid for Herbig-Haro 1. The differences between the conclusions of this analysis and those of Hartigan (1989), who made a similar study of the Mach disk in HH 1, are almost entirely due to the latter's neglect of the possibility that the ambient gas may itself be moving away from the jet source at a significant velocity.

Using equations (22) and (23), one can show that the ratio of the perpendicular cooling distance behind the bowshock $d_\perp^{\rm BS}$ to that of the Mach disk $d_\perp^{\rm MD}$ is

$$\frac{d_\perp^{\rm BS}}{d_\perp^{\rm MD}} = \frac{n_{\rm jet}}{n_0}\left(\frac{v_{\rm BS}}{v_{\rm MD}}\right)^4 = \beta_{\rm jet}\left(\frac{v_{\rm BS}}{v_{\rm MD}}\right)^6 , \qquad (25)$$

where the second equality follows from momentum conservation. Here, $v_{\rm BS}$ and $v_{\rm MD}$ denote the perpendicular shock speeds of the bowshock and Mach disk (which are both assumed to be larger than 66 km s^{-1}), $n_{\rm jet}$ is the number density in the jet and $\beta_{\rm jet}$ represents the fraction of the jet momentum that goes into accelerating the ambient gas, rather than being diverted sideways, which typically has a value $\beta_{\rm jet} \simeq 0.7$ Hartigan (1989). If the physical velocities of the jet, working surface and ambient medium are denoted by, respectively, $u_{\rm jet}$, $u_{\rm WS}$ and $u_{\rm env}$, then we can write $v_{\rm BS} = u_{\rm WS} - u_{\rm env}$ and $v_{\rm MD} = u_{\rm jet} - u_{\rm WS}$. Hence, in order that the cooling distance behind the Mach disk be longer than that behind the bowshock, we have the approximate condition

$$u_{\rm jet} \geq 2u_{\rm WS} - u_{\rm env} , \qquad (26)$$

where $\beta_{\rm jet}^{1/6} \simeq 1$ has been assumed.

For Herbig-Haro 1, $u_{\rm WS} = 300$–380 km s^{-1}from proper motion measurements, whereas $u_{\rm jet}$ cannot reasonably much exceed 500 km s^{-1}. Hence, from equation (26), we require that $u_{\rm env} > 200$ km s^{-1}. That the ambient medium has such a velocity in HH 1 is strongly indicated by other studies, see the discussion in § *6.2.* On the other hand, we really require, not only that $d_\perp^{\rm MD}$ exceed $d_\perp^{\rm BS}$, but that it be comparable to the size of the bowshock. In HH 1, taking $u_{\rm WS} = 350$ km s^{-1}, $u_{\rm jet} = 500$ km s^{-1}and $u_{\rm env} = 200$ km s^{-1}, we find $v_{\rm BS} = 150$ km s^{-1}and $v_{\rm MD} = 200$ km s^{-1}. Hence, in order that the Mach disk cooling length be significant (here, taken to mean $> 2 \times 10^{-3}$ pc) we need $n_{\rm jet}$ to be less than 300 cm^{-3}. This is roughly a factor of two less than the value of $n_{\rm jet}$ estimated by Hartigan (1989). The

above analysis also implies that the ambient density n_0 should be less than 500 cm^{-3}, whereas analysis of the upstream scattered light leads to a value of order 1000 cm^{-3} (Henney, Raga, & Axon 1994). However, the large uncertainties in all these estimations render the significance of the conflict doubtful. Nevertheless, it should be borne in mind when considering the results presented in subsequent sections that in some HH objects there may also be a contribution to the emission from the Mach disk, which is not considered. If there is strong cooling behind the Mach disk, then it will also affect the pressure distribution in the cocoon of shocked jet gas. In such a case, it is not clear that the pressure distribution adopted here [equation (6)] is at all appropriate. However, to deal with this point in a satisfactory manner would require detailed hydrodynamic calculations, which are beyond the scope of this study.

3.2. Velocity of the Emitting Gas

As discussed in the previous section, the gas is assumed to cool promptly behind the bowshock, so that the normal component of the postshock gas velocity in the frame of the shock is zero. The postshock velocity of the emitting gas *in the stationary frame of the upstream gas* is then

$$\mathbf{u}_1 = u_0(\mathbf{k}.\hat{\mathbf{n}})\hat{\mathbf{n}} = \frac{u_0(g_x\mathbf{i} + g_y\mathbf{j} + \mathbf{k})}{1 + g_x^2 + g_y^2} \quad . \qquad (27)$$

Expressions for the partial shape derivatives g_x and g_y for Case 1 and Case 2 are rather cumbersome but straightforward to calculate.

The true nature of the flow in the cooling region behind the bowshock cannot be accurately captured by the simple model developed here. However, in lieu of a more complicated model, it is useful to consider the addition of a thermal and a turbulent component to the velocity given by equation (27). The thermal component depends on the mean temperature of the gas in the line-emitting region and on the atomic weight of the ion and will hence vary from emission line to emission line, being larger for high excitation lines and for hydrogen. However, shock models show that for a given line this temperature is often not strongly dependent on the shock velocity (Hartigan, Morse, & Raymond 1994). Hence, it can be taken to be constant across the bowshock and included by a simple convolution of the resultant emission line profiles with a Gaussian of the appropriate width. The turbulent component is less well constrained but, if the turbulence is assumed to be excited by shear instabilities (e.g., Kelvin-Helmholtz), then it is reasonable to assume that it is proportional to the parallel post-shock velocity w (see § *3.1.*). The turbulent velocity is hence taken from an isotropic Gaussian distribution, with width ηw, where η is an adjustable parameter. This is easily incorporated within the framework of the probabilistic method of calculating the emission.

4. EMISSION LINE IMAGES

In this section we present monochromatic images of the bowshock models in the light of particular optical emission lines. The emission lines chosen are [S II] 6716+6731, Hα and [O III] 4959+5007, covering the range from low to high excitation. The images are calculated using a "patchwork" of planar radiative shock models (Hartigan et al. 1987). Full pre-ionization of the preshock gas is assumed in all cases. In order to produce the images, apart from the physical parameters discussed in § 2, the orientation of the bowshock with respect to the observer must also be considered. This is specified by two angles: α, the inclination of the z-axis with respect to the plane of the sky, and β, the angle which the x-axis has been rotated from the plane of the sky about the z-axis. These are illustrated in Figure 6. Hence, the projected position $[x', y']$ on the plane of the sky of a bowshock element at position $[x, y, z]$ is given by

$$x' = -x\sin\alpha\sin\beta - y\sin\alpha\cos\beta + z\cos\alpha \quad , \qquad (28)$$

$$y' = x\cos\beta - y\sin\beta \quad . \qquad (29)$$

The first group of three figures all show bowshock models with a speed $u_0 = 150$ km s^{-1}that are either

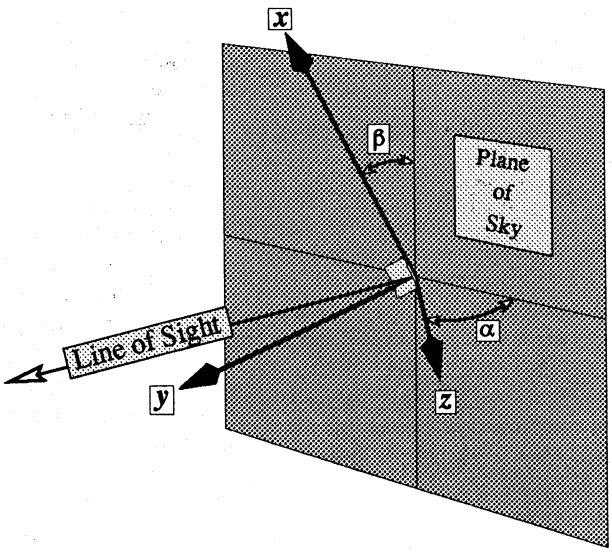

Fig. 6. Orientational parameters of the models: α is the angle between the jet axis and the plane of the sky, β is the rotation about this axis of the density gradient axis, measured from the plane of the sky.

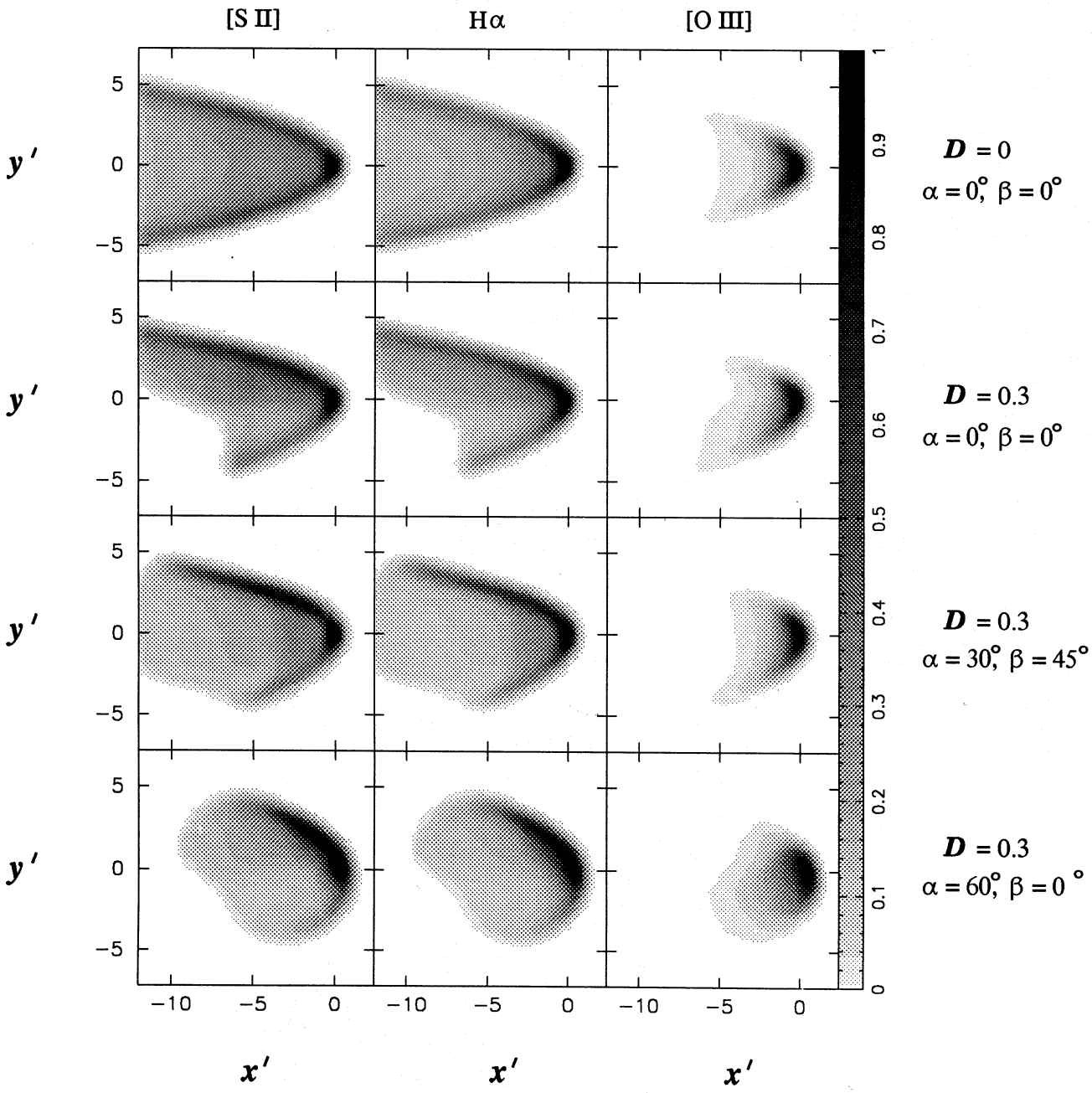

Fig. 7. Emission line images of paraboloid bowshocks ($\dot{\xi} = 1$) moving into uniform and non-uniform media. Lines shown are [S II] 6716+6731 (left column), Hα (middle column) and [O III] 4959+5007 (right column). All models have a bowshock velocity $u_0 = 150$ km s^{-1}. Density gradient and orientation parameters are indicated to the right of each row. The grayscale is linear and is normalized to the peak flux of each image. Ratios of peak flux in [S II] to peak flux in Hα are (top to bottom) 0.44, 0.45, 0.45, 0.48. Ratios of peak flux in [O III] to peak flux in Hα are (top to bottom) 2.20, 2.24, 2.17, 1.31. A seeing width of 0.5 is assumed.

symmetrical (Case 0) or have an ambient density gradient (Case 1). Figure 7 shows images of paraboloid bowshocks ($\xi = 1$) in the light of each of the three emission lines. The top row shows a symmetrical model moving in the plane of the sky. The next three rows all show a model with an ambient density gradient $\mathcal{D} = 0.3$, at various orientations to the line of sight, as indicated on the figure. Figures 8 and 9

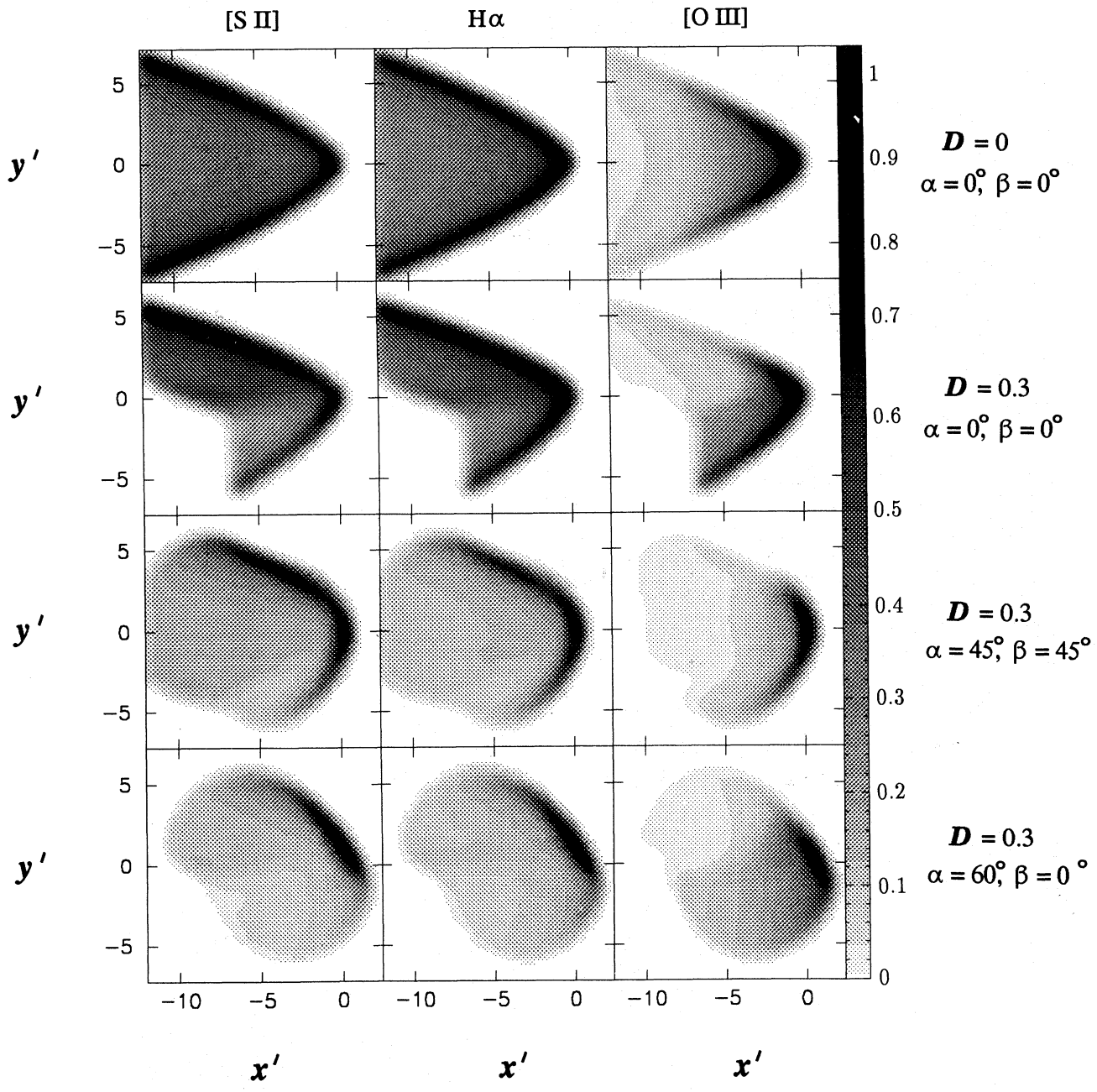

Fig. 8. Emission line images of pointed bowshocks ($\xi = 0.5$) moving into uniform and non-uniform media. Otherwise, the same as Figure 7. Ratios of peak flux in [S II] to peak flux in Hα are (top to bottom) 0.43, 0.49, 0.41, 0.47. Ratios of peak flux in [O III] to peak flux in Hα are (top to bottom) 2.29, 2.27, 2.26, 1.10. A seeing width of 0.5 is assumed.

show exactly equivalent groups of models but with $\xi = 0.5$ and $\xi = 2.0$, respectively, leading, in the first instance, to more pointed bowshock shapes that are asymptotically conical and, in the second instance, to blunter bowshock shapes with flat "noses".

It is apparent from the figures that the zone of [O III] emission is much less extended than that of [S II] or Hα. This is because the higher postshock temperatures needed for the production of O III are only found behind the relatively high velocity shocks close to the front of the bowshock. The most important feature to note about the models with an

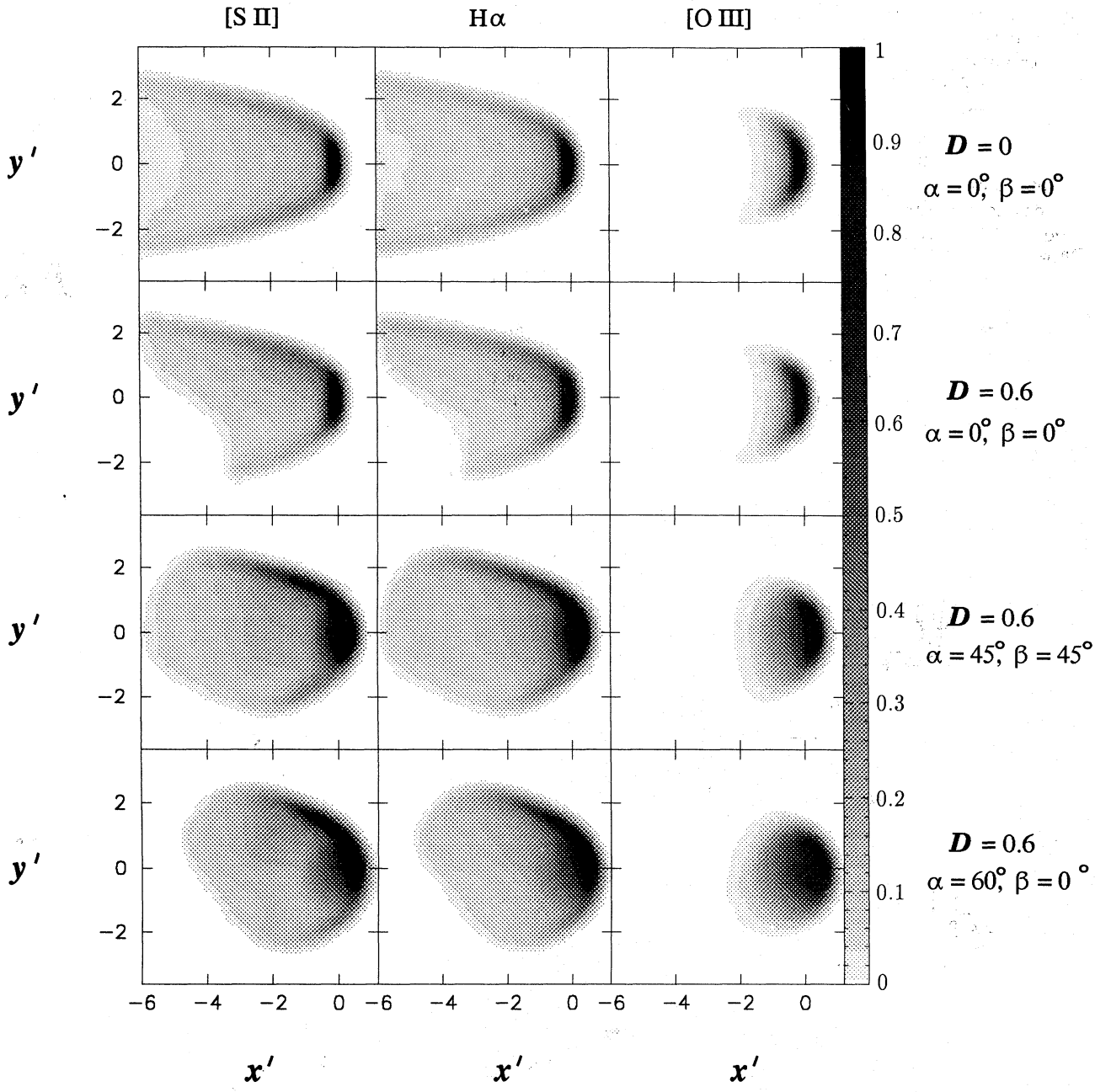

Fig. 9. Emission line images of blunt bowshocks ($\xi = 2.0$) moving into uniform and non-uniform media. Otherwise, the same as Figure 7. Ratios of peak flux in [S II] to peak flux in Hα are (top to bottom) 0.48, 0.48, 0.46, 0.48. Ratios of peak flux in [O III] to peak flux in Hα are (top to bottom) 2.05, 2.05, 1.94, 1.44. A seeing width of 0.25 is assumed.

ambient density gradient is that the asymmetry in the low excitation lines ([S II] and Hα) is opposite in sense to that in the high excitation lines ([O III]). That is, the low excitation lines are brighter from the high density side (top in the figures), whereas the high excitation lines are brighter from the low density side. This is because the velocity dependence of the [O III] is very steep, so that the decrease in density is more than made up for by the more open shape of the bowshock, which leads to a slower decrease in perpendicular shock velocity towards the wings. The low excitation lines, on the other hand, are not

so sensitive to shock velocity and so the higher mass flux of gas through the shock on the high density side leads to them being brighter there. It can be seen that this state of affairs is quite robust to variations in the model parameters and orientation, although it is less pronounced in the blunter bowshock model ($\xi = 2$, Fig. 9), since the [O III] emission is so concentrated towards the nose in this case. Figure 10 shows the effect of varying the speed of the bowshock with respect to the upstream gas. For the low velocity model, the [O III] emission is weaker and more localised while the [S II] emission is more prominent, especially on the high density side. For the high velocity model, on the other hand, [O III] is much stronger and extends further towards the wings because of the higher shock velocities. The general pattern of asymmetry remains the same, however, and it is probably safe to assert that such a dichotomy between the asymmetry in the distribution of low and high excitation emission is a general feature of steady state bowshocks propagating into a medium with a transverse density gradient.

A selection of Case 2 (skew jet pressure) models is shown in Figure 11. It can be seen that, unlike in Case 1, these models all show the same sense of asymmetry for all the emission lines. That is, the emission is always brighter from the higher pressure side (downwards in the figure). This is because, with a constant upstream density, the only factor influencing the emission is the bow shape and hence the run of perpendicular shock velocity with position. Since, for full preionization, line emissivity is a monotonically increasing function of velocity in the relevant range, the more open side of the bowshock is always the brighter.

5. EMISSION LINE PROFILES

In this section, simulated longslit spectrograms are presented that show the predicted line profiles from the models as a function of position along a slit. The positions of the two slits used are shown in Figure 12, superimposed on an example model image of the bowshock. Slit A runs along the x'-axis, parallel to the projection of the jet axis onto the plane of the sky, while Slit B runs parallel to the y'-axis, displaced downstream from the head of the bowshock by 6 units ($\xi = 0.5, 1$) or 3 units ($\xi = 2$). Spectrograms are shown in Figures 13 to 18 for the Hα line and for the line ratios [S II]/Hα and [O III]/Hα.

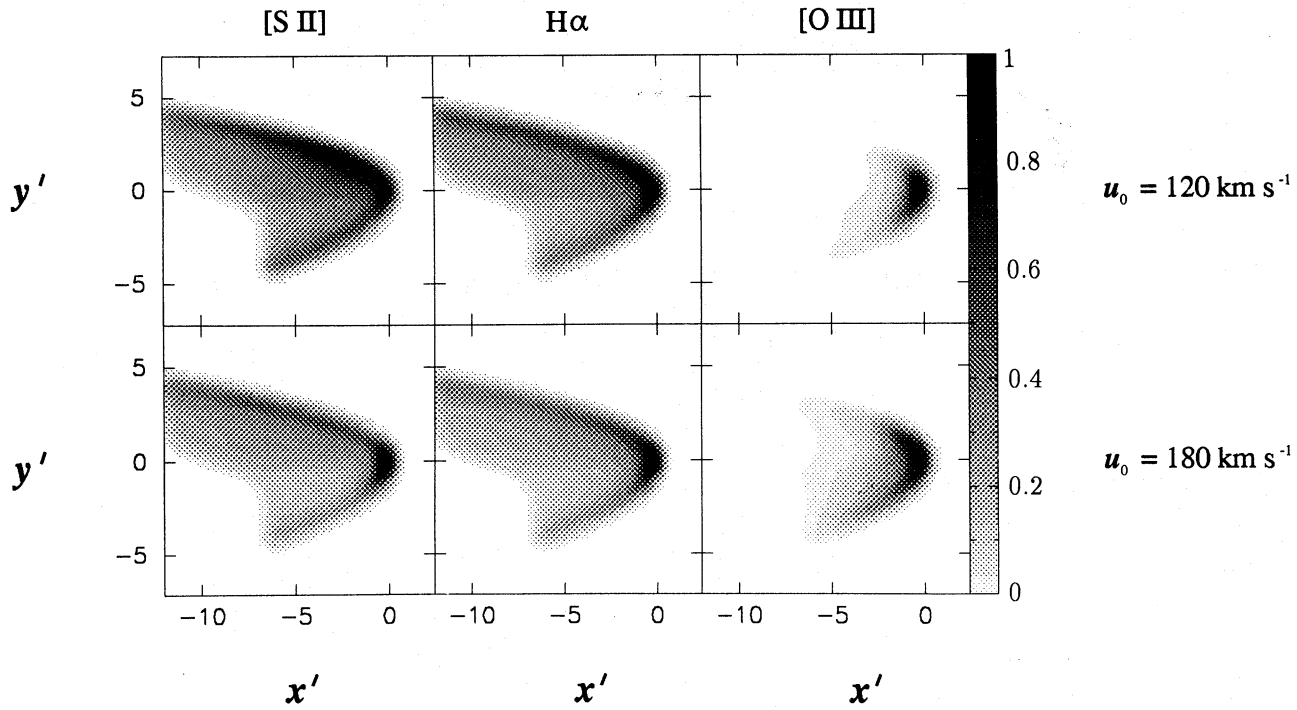

Fig. 10. Emission line images of paraboloid bowshocks moving into a non-uniform medium. The top row shows a slower bowshock than in the previous figures while the bottom row shows a faster bowshock. Bowshock speed is indicated to the right of each row. All models have $\xi = 1$, $\mathcal{D} = 0.3$, $\alpha = \beta = 0.0$. Ratios of peak flux in [S II] to peak flux in Hα are (top to bottom) 0.40, 0.49. Ratios of peak flux in [O III] to peak flux in Hα are (top to bottom) 2.26, 2.00. A seeing width of 0.5 is assumed.

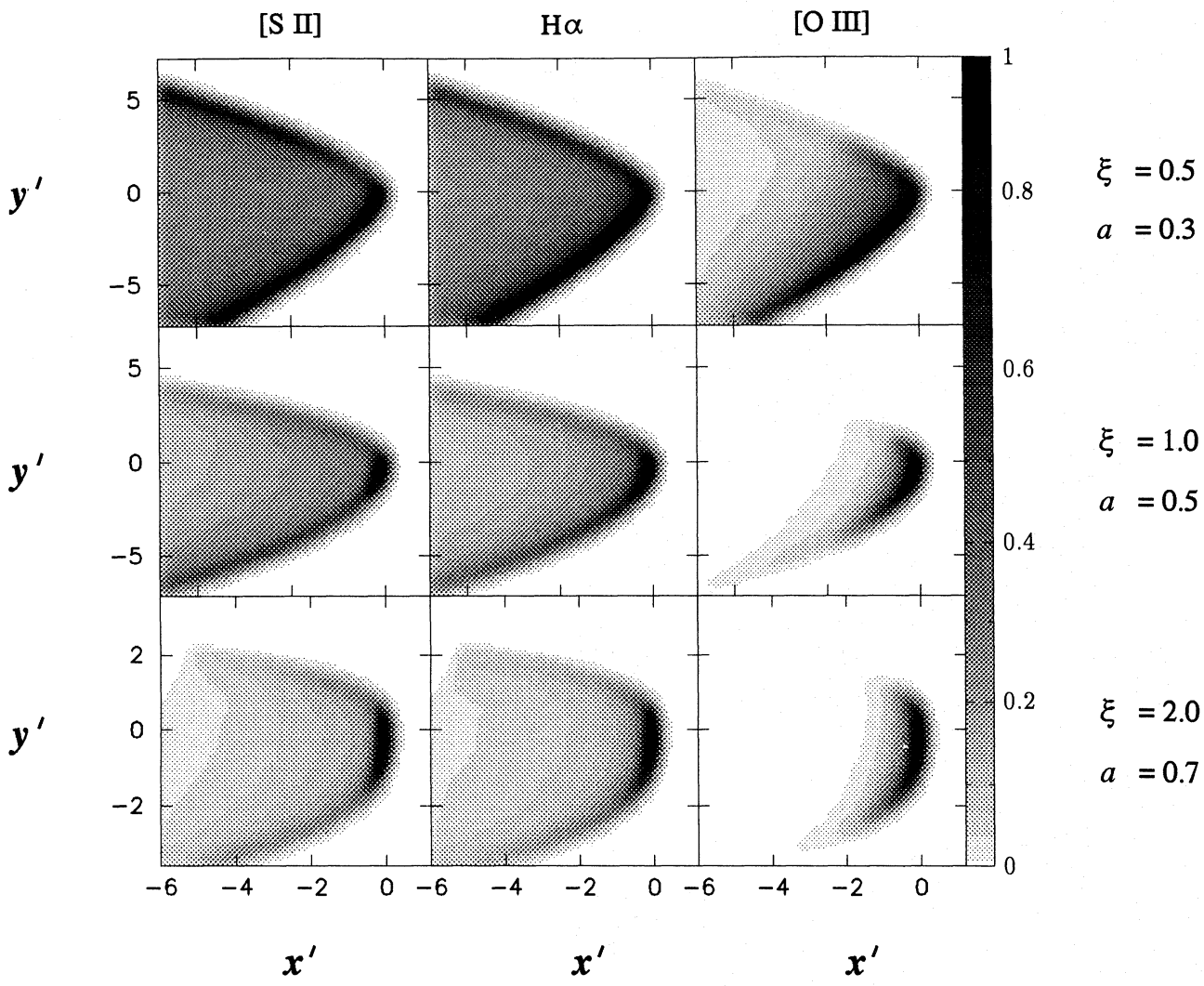

Fig. 11. Emission line images of bowshocks driven by a skew jet pressure distribution. Lines shown are as in Figure 7, and all models have $u_0 = 150$ km s^{-1} and are moving in the plane of the sky ($\alpha = \beta = 0$). Jet pressure steepness and skewness parameters are indicated to the left of each row. Ratios of peak flux in [S II] to peak flux in Hα are (top to bottom) 0.43, 0.45, 0.48. Ratios of peak flux in [O III] to peak flux in Hα are (top to bottom) 2.36, 2.18, 2.04.

Figure 13 shows aperture A spectra for the model whose images appear in Figure 7. All are paraboloid bowshocks ($\xi = 1$), moving at 150 km s^{-1}into an ambient medium with density gradient $\mathcal{D} = 0.3$. No turbulent broadening has been included in these spectra. The top left three panels show the model seen from a direction such that both the jet axis and the density gradient lie in the plane of the sky ($\alpha = \beta = 0$). In this case, a symmetrical line profile is seen since the slice of the bowshock whose light enters the slit is perpendicular to the density gradient and hence is itself symmetrical. At the very tip of the bowshock, the postshock velocity is in the plane of the sky and hence the Doppler shift is zero. However, moving back from the tip, the angle between the postshock velocity and the jet axis increases while the magnitude of the postshock velocity simultaneously decreases. For $\alpha = 0$, this leads, independently of the bowshock shape, to a maximum Doppler shift of $\pm 0.5 u_0$ when $\theta = 45°$ (where θ is the angle between the normal to the bowshock surface and the jet axis). For $\xi = 1$, this maximum Doppler shift occurs at $x' = -0.5$ and can be clearly seen in the Hα spectrogram.

The line ratio spectrograms reflect the behaviour of each line ratio as a function of shock velocity. The [S II]/Hα ratio has a broad minimum around 100 km s^{-1}, rising for higher and lower velocities, but then

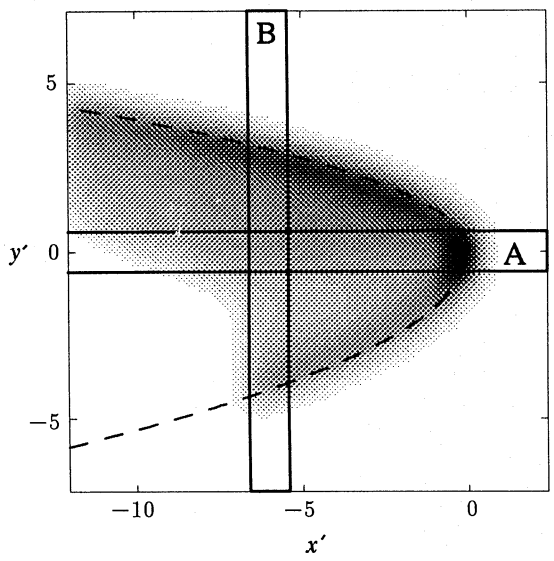

Fig. 12. Positions of the slits A and B, for which simulated spectrograms are presented, shown superimposed on an image of a typical model. The outline of the bowshock is indicated by the dashed line.

falling again below 40 km s^{-1}. The [O III]/Hα ratio, on the other hand has a maximum around 100 km $s^{-1}$and falls to very low values for shock speeds less than 80 km s^{-1}. Hence the maxima in [O III]/Hα and minima in [S II]/Hα in the region just behind the head of the bowshock. Note that the [S II] lines are narrower than either [O III] or Hα because of the lower thermal broadening, a result of the high atomic weight of sulfur combined with the low temperature of formation of the lines.

It can be seen from the figure that the effect on the Hα line shape of an inclination of the density gradient (top right panels) is in some ways similar to that of a moderate inclination of the jet axis (bottom left panels). That is, both induce an enhancement in the intensity of the blue wing of the line, together with a slight hook in the spectrogram profile on the blue side. (For the sake of clarity, in this discussion it is assumed that the inclination angle is positive in either case. If it is negative, then the same reasoning holds, but with "red" and "blue" reversed). However, the behaviour of the line ratios is quite different in the two cases. For the case of an inclined density gradient ($\beta > 0$), the blue part of the line profile comes from a region of the bowshock with higher preshock density and lower shock velocity than the red part at the same value of x'. Hence, the [S II]/Hα ratio increases and the [O III]/Hα ratio decreases towards the blue. For the case of an inclined jet axis ($\alpha > 0$), however, the blue part of the line comes from closer to the head of the bowshock than the red part, and hence the [S II]/Hα ratio decreases and the [O III]/Hα increases towards the blue. The two cases can therefore be easily distinguished observationally.

Figure 14 shows the same spectra but including a turbulent velocity dispersion in the post-shock gas (see § *3.2.*). It can be seen that the appearance of the spectrograms is substantially changed, especially away from the head of the bowshock, where the parallel postshock velocity is large and the turbulent broadening causes the red and blue branches of the line profile to merge into a single broad component. The pattern of the line ratios, however, remains essentially unchanged and the comments made in the previous paragraph regarding the distinction between an inclined jet axis and an inclined density gradient still hold.

Figures 15 and 16 show aperture B spectra for the same models as the previous figures, respectively without and with the inclusion of turbulent broadening. For $\alpha = 0$ (top panels), the spectrograph slit cuts the bowshock perpendicular to its axis and hence the emission lines form closed loops in the vy'-plane. With this aperture, the effects of the ambient density gradient can be seen directly, even when it is in the plane of the sky ($\beta = 0$). The denser side ($y' > 0$) is brighter in Hα, with a smaller velocity difference between the red and blue components and a smaller [O III]/Hα ratio. Tilting the density gradient (top right panels) rotates all these effects around the loop of the line. Tipping the bowshock axis (lower panels) only slightly modifies the line shapes. More noticeable is the fact that the loops are incomplete, caused by the slit missing the back side of the bowshock because emission is only calculated up to a fixed cylindrical radius. When turbulent broadening is included, the loop is smeared into a line, giving a single broad velocity component at each position. However, where the two original components arose from regions of different excitation, this is still apparent in the line ratios of the broadened spectra (top right panels).

Figure 17 shows aperture A spectra for models with different values of ξ, with no turbulent broadening, while Figure 18 shows the same models with turbulent broadening. It can be seen that the bowshock shape quite strongly affects the spectra, especially near the head. With the pointier bowshock moving in the plane of the sky (top left), the line splits into two components immediately and there is a minimum at zero Doppler shift, even at $x' = 0$. The blunter bowshock (bottom left), on the other hand, has the emission at the head concentrated at zero Doppler shift. When the bowshock axis is tipped, however (right hand panels), the maximum intensity in the pointed model comes from the back side of the bow, close to zero velocity, whereas the maximum intensity in the blunt model comes from the near side of the bow, in the blue-shifted part of the profile.

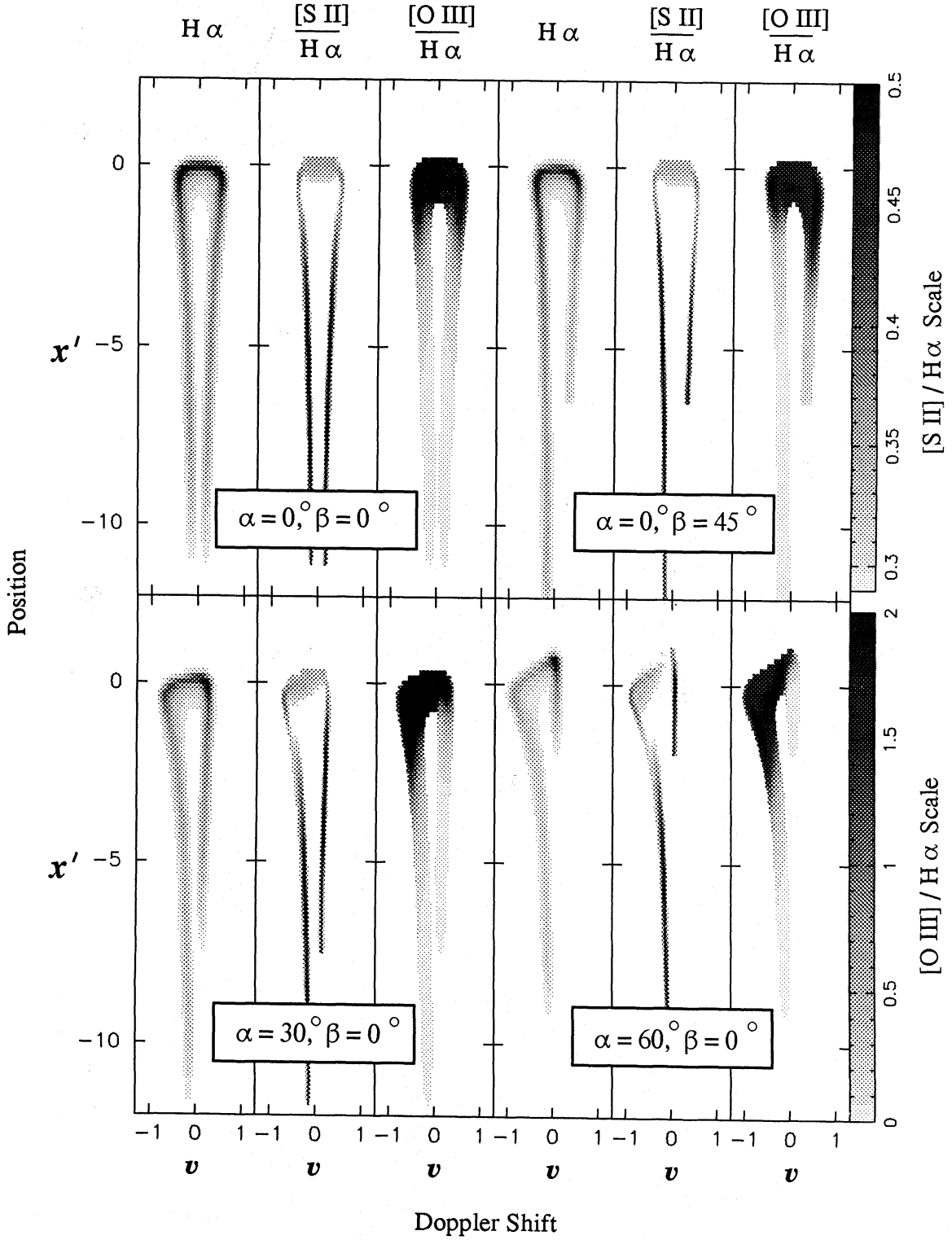

Fig. 13. Example spectrograms from aperture A, with no turbulent broadening. All are for models with $\xi = 1$, $\mathcal{D} = 0.3$, $u_0 = 150$ km s^{-1}. Three position-velocity diagrams are shown for each orientation: intensity of Hα; ratio of [S II] to Hα, and ratio of [O III] to Hα. The scale is linear in each case and for the line ratios is indicated to the right of the figure. The Doppler shift scale is in units of the bowshock speed u_0. A seeing width of 0.1 and a velocity resolution of 0.05 (7 km s^{-1}) are assumed.

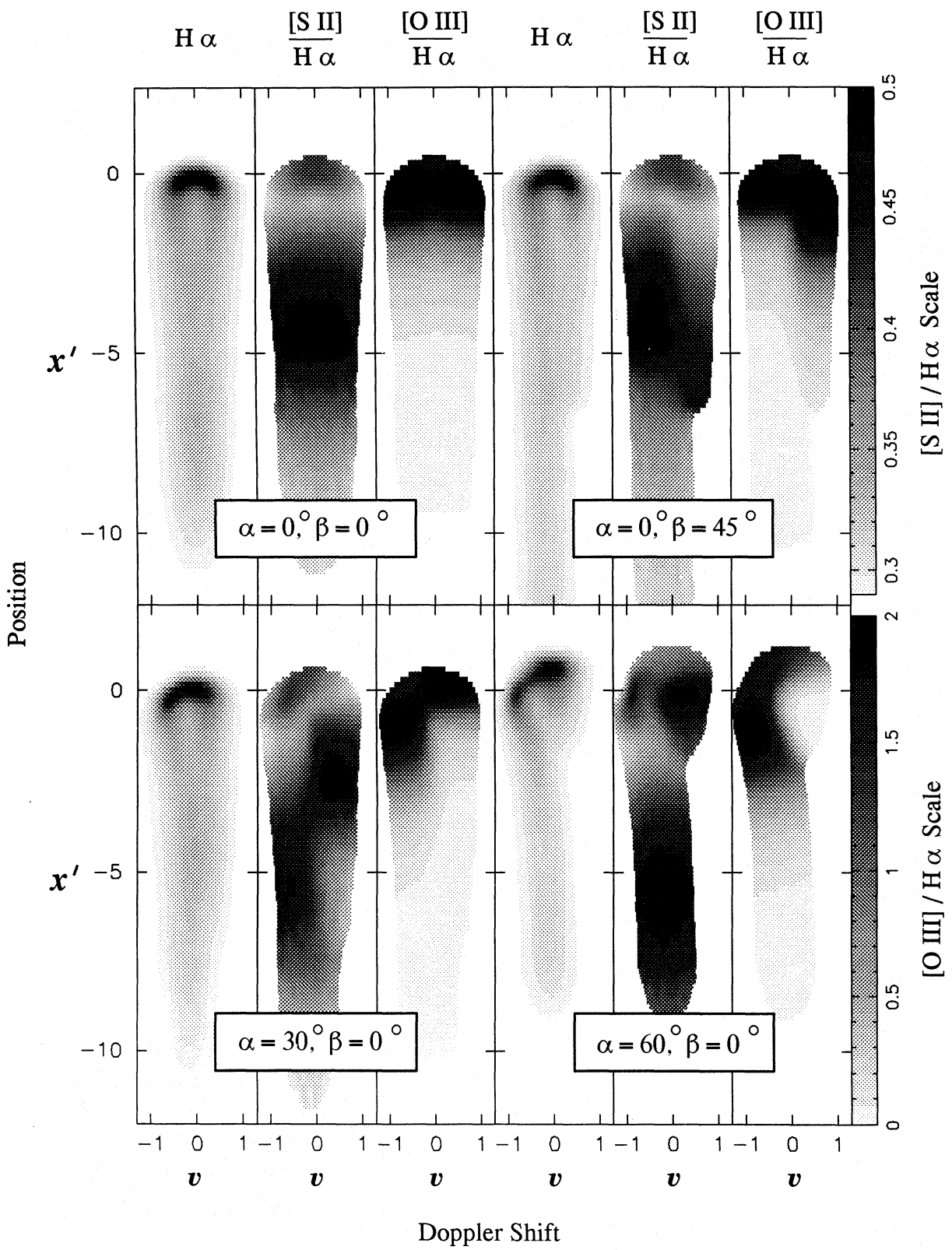

Fig. 14. Example spectrograms from aperture A, with turbulent broadening $\eta = 0.3$. A seeing width of 0.25 and velocity resolution of 0.1 (15 km s^{-1}) are assumed. Otherwise, the same as Figure 13.

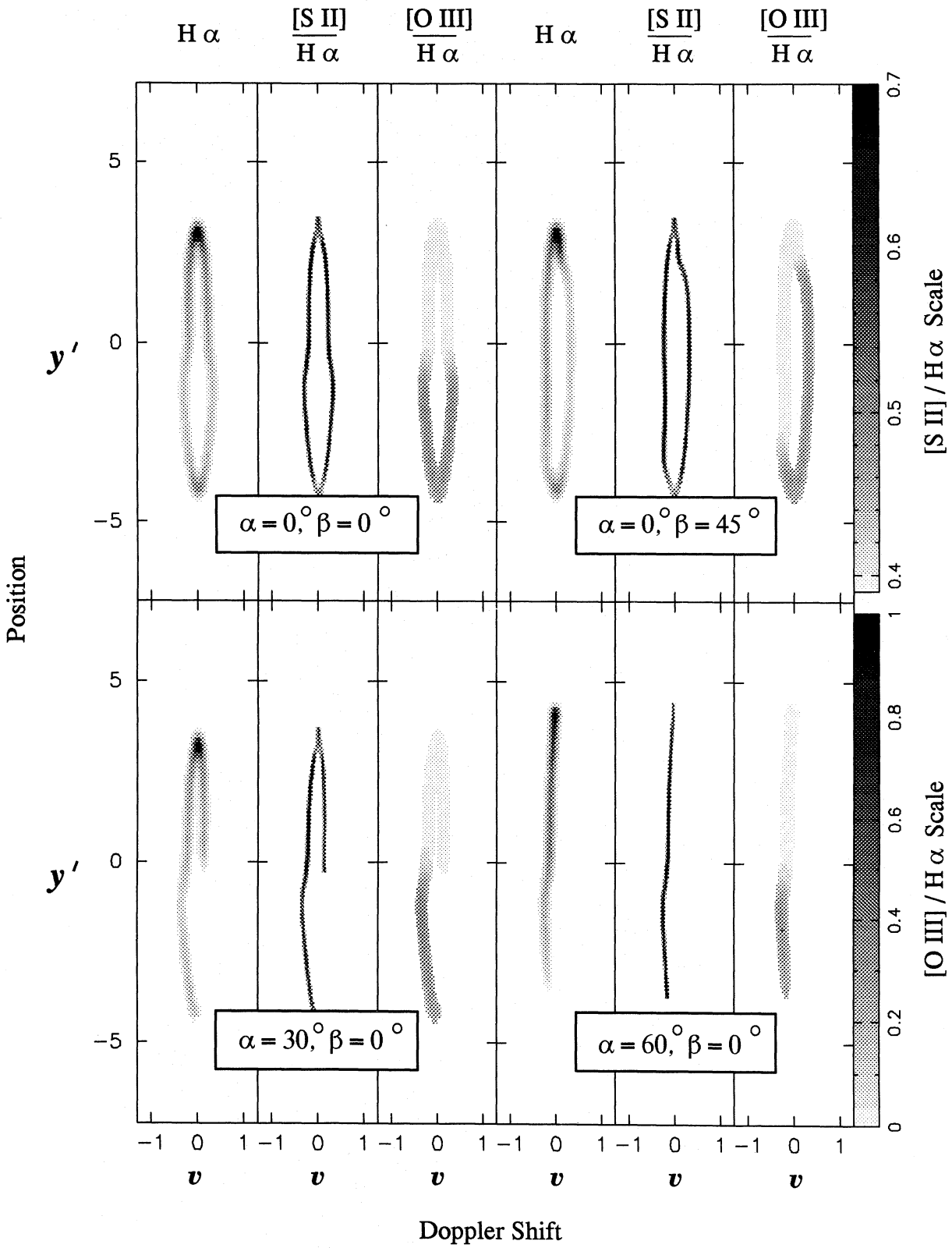

Fig. 15. Example spectrograms from aperture B, without turbulent broadening. Otherwise, the same as Figure 13.

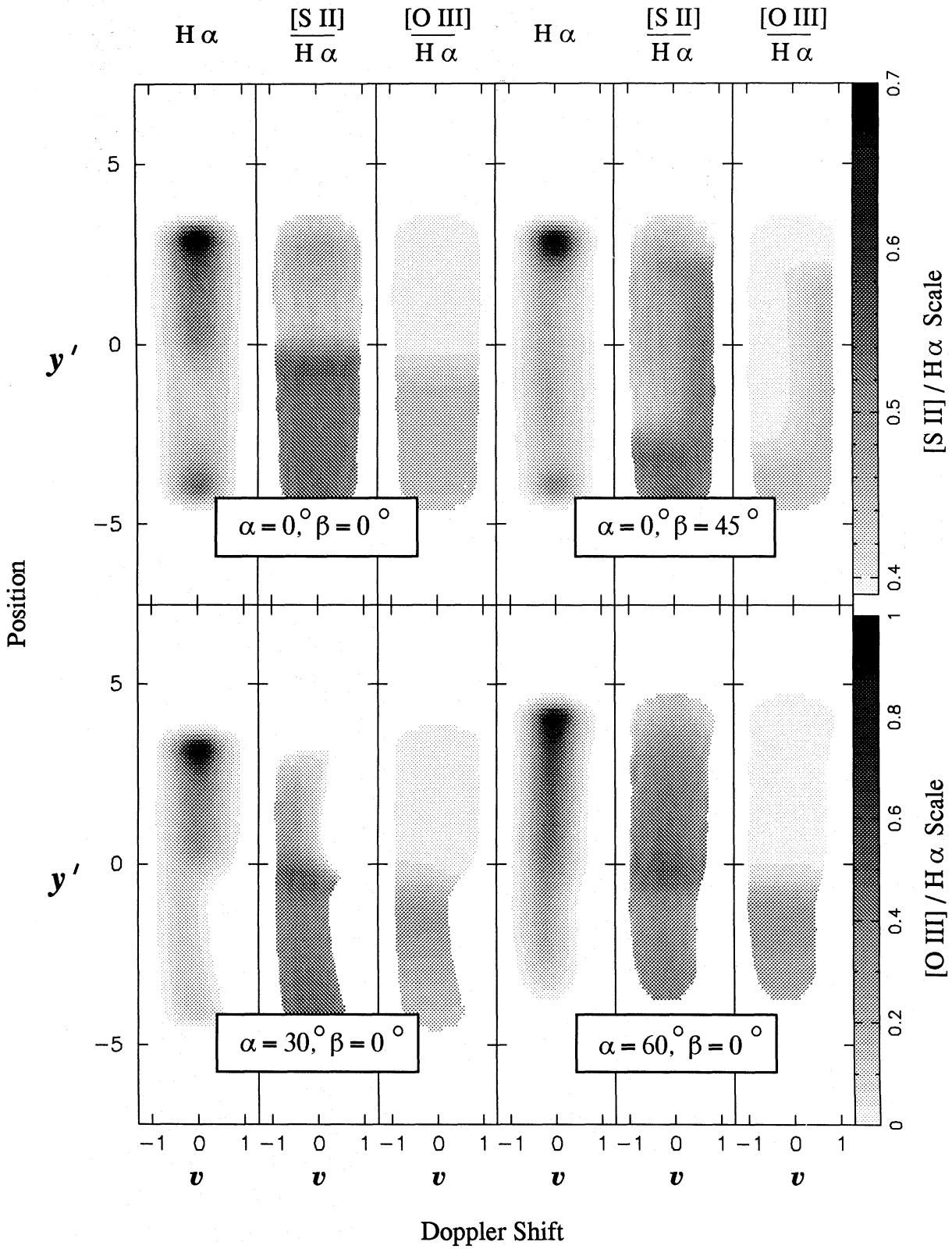

Fig. 16. Example spectrograms from aperture B, with turbulent broadening $\eta = 0.3$. Otherwise, the same as Figure 14.

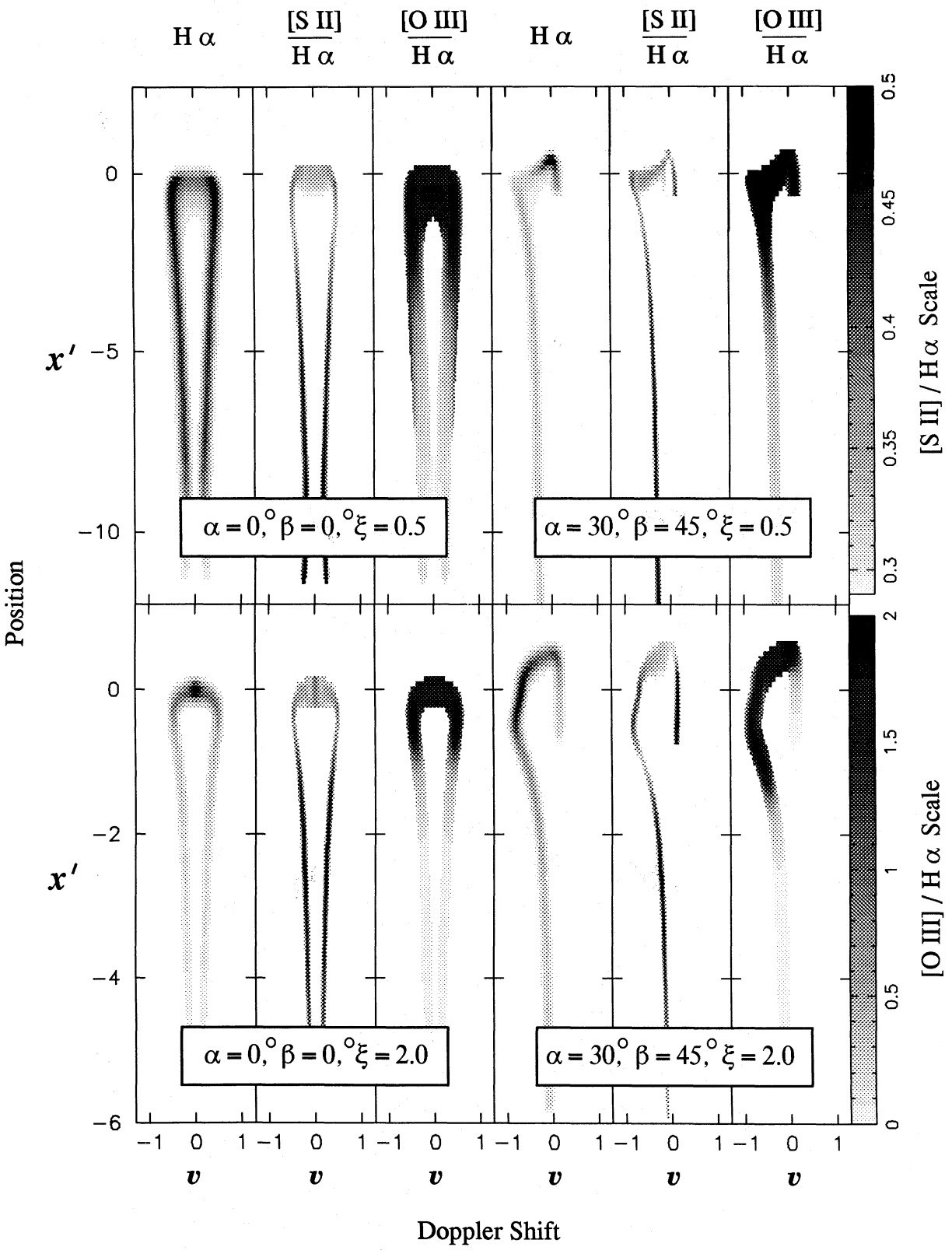

Fig. 17. Example spectra from aperture A for different shapes of bowshock, with no turbulent broadening. Otherwise, the same as Figure 13.

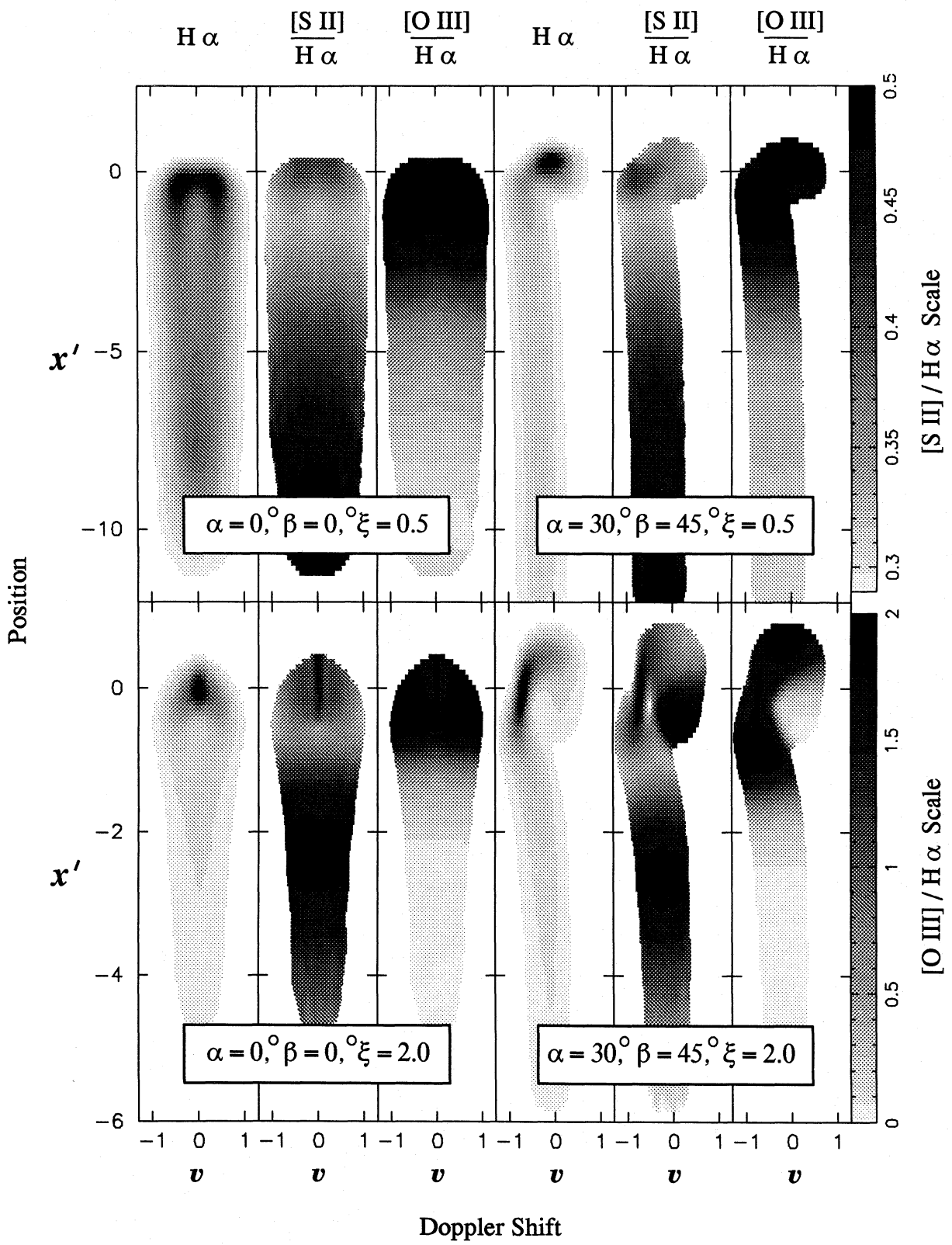

Fig. 18. Example spectra from aperture A for different shapes of bowshock, turbulent broadening $\eta = 0.3$. Otherwise, the same as Figure 14.

The effects on the two models of the turbulent broadening (Fig. 18) are also quite different. Since, in the pointed model, the parallel postshock velocity varies only slowly with position in the regions that contribute most to the line profile, the smearing due to the turbulent broadening is roughly constant along the length of the slit. With the blunt model, however, the intensity maximum at the head of the shock is relatively unbroadened since the shock is virtually perpendicular there. This results in a clear separation in the spatially integrated line profile of a narrow component from the head and a broad component fom the wings.

6. DISCUSSION

In this section, we discuss the application of the models presented in this paper to the interpretation of Herbig-Haro bowshocks. The discussion is rather qualitative since the models have not been tailored to particular objects. A future paper will present detailed quantitative comparisons between spectroscopic observations of HH 1 and specific models, including the effects of emission line scattering by surrounding dust (see Henney 1995 for preliminary results).

6.1. Possible Mechanisms for Generating Asymmetric Bowshocks

All Herbig-Haro bowshocks that have been observed in any detail show some evidence for departures from cylindrical symmetry. In some objects, such as HH 111 (Reipurth et al. 1992), these asymmetries are rather slight, while in others, such as HH 1 (Solf et al. 1991; Eislöffel et al. 1994; Hester et al. 1995), HH 34 (Morse et al. 1992) and HH 47 (Morse et al. 1994), they are more spectacular. Various explanations for the asymmetries have been proffered, which can be usefully divided into three classes.

Firstly, there is the possibility that clumpiness in the ambient gas or thermal instabilities in the postshock flow (Raga et al. 1988) lead to bright knots of emission, with lifetimes of the order of the bowshock's dynamic timescale. If these clumps are few enough in number then, although the bowshock may be symmetric in a time-averaged sense, at any particular time it will appear brighter on one side than the other. For example, suppose that the bowshock emission is dominated by that of the knots, that all knots are of equal brightness and that the appearance of each knot is uncorrelated with that of any other knot. Further, suppose that at any one time there are an average of $\bar{N}$ knots present and that the bowshock is divided into two equal halves, such that there is an average of $\bar{N}/2$ knots present in each half. Then, by summation over two independent Poisson distributions of mean $\bar{N}/2$, it is straightforward to show that the mean ratio of the intensity of the dimmer half to that of the brighter half will be less than 0.5 so long as $\bar{N}$ lies between about 0.95 and 4.7. This estimate, though admittedly crude, suggests that, given their observed clumpiness, one would expect roughly half of all bowshocks to show a brightness asymmetry between their two sides of a factor of two or greater owing to this mechanism alone.

Secondly, the shape of the bowshock could be affected by periodic variations in the source of the driving jet. A "wiggling" or precessing jet (Raga & Biro 1993; Biro 1994) would produce a non-axisymmetric bowshock at its head, which would vary in form in a complicated time-dependent way. The models with a skew jet pressure discussed in this paper (Case 2) are an attempt to investigate within a steady-state framework the possible consequences of such a time-varying jet. In some objects, such as HH 46/47 (Reipurth & Heathcote 1991), the sinusoidal pattern of the knots of the jet itself lend credibility to this mechanism. In many other objects, however, angular variations are either very small or absent.

Lastly, the explanation for asymmetry of the bowshock may lie in systematic asymmetries in the environment into which the jet is propagating. The models in this paper with a transverse density gradient (Case 1) illustrate an example of this class of explanation. Of course, if the the density perturbation is large enough in amplitude and in spatial extent, then it will have serious consequences for the propagation of the jet that is driving the bowshock, causing it to be deflected from its original path (Raga & Cantó 1995). However, the density contrast considered here, although producing marked effects in the bowshock emission, is only ~ 3.5 and hence would not measurably affect the jet.

It is probable that all three of these explanations play some role in generating the observed asymmetries, with perhaps more than one mechanism acting at the same time in some cases. We now turn to a particular object, HH 1, and investigate in greater detail the relevance of the above three mechanisms.

6.2. HH 1

Images of HH 1 taken through red continuum or emission line filters between 1947 and the present (Herbig 1951; Herbig & Jones 1981; Solf et al. 1991; Eislöffel et al. 1994; Hester et al. 1995) without exception show the bowshock to be asymmetric in the same sense. That is, although the brightness of individual knots changes with time, the north-east wing is consistently brighter than the south-west wing. The angular size of HH 1 is $\sim 10''$ and proper motion measurements of the leading condensation (Herbig & Jones 1981; Eislöffel et al. 1994) indicate that it has travelled roughly this same distance in the almost 50 years of observations. However, a better estimate of

the dynamical time is probably 100 years, since there is increasing evidence that the preshock gas is itself moving (Henney et al. 1994), possibly due to previous ejection events (Raga & Kofman 1992), and that the true speed of the bowshock with respect to this gas is 150–200 km s^{-1}, rather than the 300–380 km s^{-1}indicated by proper motion studies. Nevertheless, such constancy in the bowshock's asymmetry over even half of a dynamic timescale argues against any explanation in terms of a random distribution of knots. On the other hand, observations of the HH 1 jet (Mundt, Brugel & Buehrke 1987; Rodríguez et al. 1990) show no evidence that its direction has been anything other than constant with time, ruling out the second class of explanations of the previous section.

The case for the third possibility, that of a density gradient in the preshock gas, is considerably strengthened by by the fact that observations of the bowshock in the light of [O III] emission do show an asymmetry opposite in sense to that seen in the low-excitation lines (Raga et al. 1988; Hester et al. 1996), just as predicted by the Case 1 models presented here (see § 4). Further evidence for a transverse density gradient in the upstream gas is furnished by the distribution of dust-scattered light upstream of the shock (Solf & Böhm 1991) and the fact that molecular hydrogen emission is only seen in the north-east wing (Noriega-Crespo & Garnavich 1994).

Turning now to the line profiles, the longslit spectrograms of Solf et al. (1991) imply that the [S II]/Hα ratio is higher in the red wing of the line than in the blue wing. If taken at face value, this would suggest a negative value of β (see § 5). That is, that the upstream density gradient is inclined in such a way that the density increases away from the observer. This would be consistent with the fact (A. Noriega-Crespo, priv. comm.) that there is no significant spatial variation in the reddening across the face of the bowshock, whereas one would expect such a variation if β were positive or zero. However, it has been suggested (Indebetouw & Noriega-Crespo 1995) that such features in the position-velocity diagrams may be artifacts caused by the misalignment of the two spectra. There certainly seems to be a strong case for this, especially with respect to the position-velocity diagram of electron density formed from the ratio of the two [S II] lines, so it is important not to over-interpret the observations. Note that the Case 1 models presented here would predict that the electron density be equal in the red and blue portions of the line profile for a bowshock moving in the plane of the sky, whatever the amplitude or orientation of the upstream density asymmetry. This is because the postshock density following cooling is proportional to the ram pressure perpendicular to the shock of the preshock gas. Since this ram pressure is balanced in our models against the cocoon pressure, which is cylindrically symmetric (§ 2), it follows that the postshock density also has cylindrical symmetry.

In summary, the results presented in this paper demonstrate that departures from cylindrical symmetry in radiative bowshocks can be investigated by means of relatively simple, analytic models. These models allow one to discriminate between different symmetry-breaking mechanisms on the grounds of their different predictions for the line ratios between high and low excitation emission lines, resolved both spatially and in velocity. In particular, models with a transverse density gradient in the upstream gas almost always show a dichotomy between their morphology in the light of high- and low-excitation emission lines. That is, the side that is brightest in [O III] is not the side that is brightest in [S II] and Hα. Hence, observation of such a dichotomy, as for instance in Herbig-Haro 1, is prima facie evidence for the existence of a density gradient in the upstream gas. This basic result is found to be largely insensitive to the form adopted for the pressure distribution in the shocked jet gas. Also, although the images and spectra presented here are for fully pre-ionized shock models, qualitatively similar results obtain if equilibrium ionization of the pre-shock gas is assumed. Another object in which preshock density gradients may be important is Cepheus A, where several asymmetric bow shocks are observed (Hartigan et al. 1986). The shock velocities in these objects, however, are much higher than in the models considered in this paper.

It is a pleasure to thank A. Raga for many helpful suggestions in the course of this work. I have also benefitted from useful discussions with S.J. Arthur, J. Hester and A. Noriega-Crespo. I thank the anonymous referee for his/her perceptive comments, which helped improve the presentation of § 3 and the Appendix.

APPENDIX

A. FORMALISM FOR CALCULATING THE BOWSHOCK EMISSION BY A MONTE CARLO TECHNIQUE

In order to minimize the variance (noise) of the resulting images and spectra, it is desirable that the probability distribution from which the photons are chosen reflect as closely as possible the actual brightness distribution of the bowshock. On the other hand, for the problem to be tractable it is also necessary that the distribution be separable with respect to the two position coordinates. In practice, these two requirements conflict and, since an excess of noise can always be cured by using more CPU time to generate more photons, the former condition is not strictly adhered to in the approach that follows.

One special case of a separable distribution, and one which is particularly easy to deal with, is where the probability distribution depends only on the cylindrical radius r. A bowshock whose intensity distribution actually followed this probability distribution would then appear circularly symmetric when seen from the front. In § *A.1.* it is shown how the coordinates of the photon origin can be found, assuming such a probability distribution, while in § *A.2.* suitable distributions are calculated for the cases discussed in § 2.

A.1. Origin of the Photons

We assume that the bowshock extends to a finite cylindrical radius r_0 and that we have a function $\Pi(r)$, which describes the probability that a photon emitted by the bowshock originates at a cylindrical radius between 0 and r and which is normalized so that $\Pi(r_0) = 1$. Then, if we have a random number ϖ_1 selected from a uniform distribution on the interval $[0, 1]$ (uniform random deviate), we can take the radius of origin of the photon to be $r = \Pi^{-1}(\varpi_1)$. Using a second deviate ϖ_2, we calculate the azimuthal angle as $\theta = 2\pi\varpi_2$, from which the Cartesian coordinates of the photon origin follow as $x = r\cos\theta$, $y = r\sin\theta$ and $z = -g(x, y)$.

A.2. Calculation of the Probability Distribution

First, we assume that the intensity of a particular emission line from the postshock gas in the bowshock can be approximated by a form

$$I = C\rho u_{\rm n}^{\alpha} \quad , \tag{30}$$

where ρ is the upstream gas density, $u_{\rm n} = -\mathbf{u}.\hat{\mathbf{n}}$ is the component of the upstream gas velocity normal to the shock and the parameters C and α are to be found. Using the results of the previous sections, we find that

$$I = CP^{\alpha/2}\rho^{(2-\alpha)/2} \quad , \tag{31}$$

which is the surface brightness of the bowshock in a particular line. More directly related to the probability distribution is the bowshock emission per unit *cross-sectional* area (by which is meant area in the xy-plane). This is given by

$$\frac{{\rm d}E}{{\rm d}x\,{\rm d}y} = Cu_0 P^{\beta}\rho^{\gamma} \quad , \tag{32}$$

where $\beta = (\alpha-1)/2$ and $\gamma = (3-\alpha)/2$. It can be seen that, in order that ${\rm d}E/{\rm d}x{\rm d}y$ be a function of r alone, we require that $\alpha = 3$ for Case 1 (ambient density gradient), or $\alpha = 1$ for Case 2 (skew pressure). With these values of α, the probability distribution is then given by

$$\Pi(r) = \int_0^r \frac{{\rm d}E}{{\rm d}x\,{\rm d}y}\,r{\rm d}r \Big/ \int_0^{r_0} \frac{{\rm d}E}{{\rm d}x\,{\rm d}y}\,r{\rm d}r \tag{33}$$

For Case 1, equation (33) is only integrable when ξ is an integer or half-integer:

$\xi = 0.5$:

$$\Pi(r) = B_0^{-1}\left[r - \ln(1+r)\right]; B_0 = r_0 - \ln(1+r_0) \ ;$$

$\xi = 1.0$:

$$\Pi(r) = B_0^{-1}\ln(1+r^2); B_0 = \ln(1+r_0^2) \ ; \tag{34}$$

$\xi = 2.0$:

$$\Pi(r) = B_0^{-1}\tan^{-1}\left(r^2\right); B_0 = \tan^{-1}\left(r_0^2\right) \ .$$

For $\xi = 1$ or 2, this equation can be inverted to give an explicit expression for the radius in terms of a uniform random deviate,

$$\begin{aligned} \xi = 1.0: &\quad r = \left[\exp(B_0\varpi) - 1\right]^{1/2} \quad , \\ \xi = 2.0: &\quad r = \left[\tan(B_0\varpi)\right]^{1/2} \quad , \end{aligned} \tag{35}$$

whereas for $\xi = 0.5$, r must be found by Newton-Raphson iteration. For Case 2, the expression for $\Pi(r)$ is much simpler and is independent of ξ. It may always be inverted to give

$$r = r_0(\varpi)^{1/2} \quad . \tag{36}$$

The velocity dependence of the post-shock line emission will in general *not* be a power law with the α dictated by the above considerations. As a result, each photon must be weighted by a factor equal to the ratio between the true velocity dependence (as determined from the shock models of (Hartigan et al. 1987) and that given by equation (30) with $\alpha = 3$ or 1, as appropriate. This weighting procedure increases the variance or "noisiness" of the results, as discussed above.

Note that, from equation (32), it is evident that, if u_0 varies with position, then there is no value of α that can ensure that ${\rm d}E/{\rm d}x{\rm d}y$ is a function of r only.

REFERENCES

Arthur, S.J., Dyson, J.E., & Hartquist, T.W. 1993, MNRAS, 261, 425

Balsara, D.S., & Norman, M.L. 1992, ApJ, 393, 631

Biro, S. 1994, Ph.D. thesis, University of Manchester

Cantó, J., & Rodríguez, L.F. 1980, ApJ, 239, 982

Cantó, J., Tenorio-Tagle, G., & Różyczka, M. 1988, A&A, 192, 287

Choe, S.-U., Böhm, K.-H., & Solf, J. 1985, ApJ, 288, 338

Dyson, J.E., & deVries, J. 1972, A&A, 20, 223
Eislöffel, J., Mundt, R., & Böhm, K.-H. 1994, AJ, 108, 1042
Haro, G. 1952, ApJ, 115, 572
Hartigan, P. 1989, ApJ, 339, 987
Hartigan, P., Morse, J., & Raymond, J. 1994, ApJ, 436, 125
Hartigan, P., Raymond, J.C., & Hartmann, L. 1987, ApJ, 316, 323
Hartigan, P., Lada, C.J., Tapia, S., & Stocke, J. 1986, AJ, 92, 1155
Henney, W.J. 1995, in Circumstellar Matter 1994, ed. G.D. Watts & P.M. Williams (Dordrecht: Kluwer), 481
Henney, W.J., & Axon, D.J. 1995, ApJ, 454, 233
Henney, W.J., Raga, A.C., & Axon, D.J. 1994, ApJ, 427, 305
Herbig, G.H. 1951, ApJ, 113, 697
Herbig, G.H., & Jones, B.F. 1981, AJ, 86, 1232
Hester, J.J. et al., 1996, AJ, submitted
Indebetouw, R., & Noriega-Crespo, A. 1995, AJ, 109, 752
Kahn, F.D. 1976, A&A, 50, 145
Martí, J., Rodríguez, L.F., & Reipurth, B. 1993, ApJ, 416, 208
Morse, J.A., Hartigan, P., Cecil, G., Raymond, J.C., & Heathcote, S. 1992, ApJ, 399, 231
Morse, J.A., Hartigan, P., Heathcote, S., Raymond, J.C., & Cecil, G. 1994, ApJ, 425, 738
Mundt, R., Brugel, E.W., & Buehrke, T. 1987, ApJ, 319, 275
Noriega-Crespo, A., & Garnavich, P.M. 1994, RevMexAA, 28, 173
Noriega-Crespo, A., Böhm, K.-H., & Raga, A.C. 1989, AJ, 98, 1388
_____. 1990, AJ, 99, 1918
Norman, C., & Silk, J. 1979, ApJ, 228, 197
Pikelner, S.B. 1968, Astrophys. Lett., 2, 97
Raga, A.C. 1985, Ph.D. thesis, University of Washington
_____. 1988, ApJ, 335, 820
Raga, A.C., & Binette, L. 1991, RevMexAA, 22, 265
Raga, A.C., & Biro, S. 1993, MNRAS, 264, 758
Raga, A.C., & Cantó, J. 1995, in The Fifth Mexico-Texas Conference on Astrophysics: Gaseous Nebulae and Star Formation, ed. M. Peña & S. Kurtz, RevMexAASC, 3, 47
Raga, A.C., & Kofman, L. 1992, ApJ, 386, 222
Raga, A.C., & Noriega-Crespo, A. 1993, RevMexAA, 25, 149
Raga, A.C., Cantó, J., Binette, L., & Calvet, N. 1990, ApJ, 364, 601
Raga, A.C., Mateo, M., Böhm, K.-H., & Solf, J. 1988, AJ, 95, 1783
Reipurth, B. 1992, in Physics of Star Formation and Pre-Main Sequence Objects, ed. C.J. Lada & N.D. Kylafis (Dordrecht: Kluwer), 247
_____. 1994, A General Catalogue of Herbig-Haro Objects. Electronically published via the World Wide Web at http://www-astro.phast.umass.edu/latex/HHcat/HHcat.html
Reipurth, B., & Heathcote, S. 1991, A&A, 246, 511
Reipurth, B., Raga, A.C., & Heathcote, S. 1992, ApJ, 392, 145
Rodríguez, L.F. 1989, RevMexAA, 18, 45
Rodríguez, L.F., Curiel, S., Ho, P.T., Torrelles, J.M., & Cantó, J. 1990, ApJ, 352, 654
Schwartz, R.D. 1975, ApJ, 195, 631
Schwartz, R.D., & Dopita, M.A. 1980, ApJ, 236, 543
Solf, J., & Böhm, K.-H. 1991, ApJ, 375, 618 (SB)
Solf, J., Raga, A.C., Böhm, K.-H., & Noriega-Crespo, A. 1991, AJ, 102, 1147

William J. Henney: Instituto de Astronomía, UNAM, Apartado Postal 70-264, 04510 México, D.F. (will@astroscu.unam.mx).